Arab American University

Faculty of Graduate Studies

Effects of gold nanosandwiching on the structural and optical properties of Copper selenide thin films

By

Tahani S A Bani Owdah

Supervisor

Prof. Atef Qassrawi

This thesis was submitted in partial fulfillment of the requirements for

The Master's degree in Physics

September /2019

Effects of gold nanosandwiching on the structural and optical properties of Copper selenide thin films
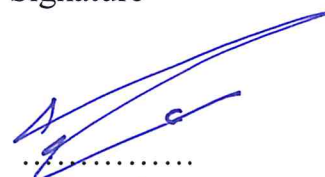
By

Tahani S .Bani Owdah

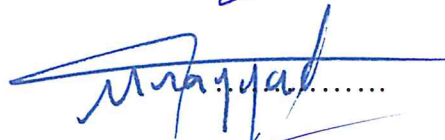This thesis was defended successfully on September 21st 2019 and approved by:

Committee members   Signature
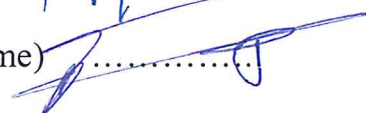
1. Prof. Dr. Atef Fayez Qasrawi (Supervisor Name)   ....

2. Dr.Muayad Abo Saa (Internal Examiner)   ....

3. Associated Prof. Iyad Saadeddin (External Examiner Name)   ....

Declaration

I certify that this work contained in the thesis is original and has been done by myself under the general supervision of my supervisor. And not been submitted elsewhere for any degree or diploma.

Acknowledgment

First of all, I thank my merciful God for giving me opportunity, hope, and strength to reach this point.

I would like to express my sincere gratitude to supervisor Prof. Dr. Atef Fayez Qasrawi whose splendid guidance, authentic supervision, assiduous cooperation, moral support and constant encouragement enabled us to make out our research problem in the present form. Thanks for Prof. Dr. Qasrawi for being a constant source of inspiration and guidance. The door to Prof. Dr. Qasrawi office was always open whenever I face a trouble spot or had a question about me research and writing.

And I sincerely thank all my D.Sc members, especially Dr. Adli Saleh, Prof. Dr. Mohammad Abu Samra, Prof. Dr. Zaki Saleh and Dr. Muayad Abu Saa.

I would like to extend my heartfelt thanks to research assistance and wonderful friend "Olfat Omareya" for ceaseless encouragement, immense help and hearty encouragement during our project work. And I would like to give special thanks to my friends especially "Nancy Yaseen" for her love, support, help and various suggestions.

I am forever indebted to my parents (Mrs. Sa'ada Daraghmeh and Mr. Salah Bani Owdah), sisters and brothers for their blessings, love, encouragement, and strong supports in every moments of my life.

I would like to give special thanks to my little niece "Reem" Twinkle who has been so refreshing and made my life enjoyable after a hectic schedule at laboratory.

Abstract

In this work, the structural and optical properties of copper selenide thin films which are prepared by the nanosandwiching technique are studied. Particularly, gold thin film layers of thicknesses less than 250 nm are used as mid-layer between two 500 nm thick copper selenide layers. The effect of the gold film on the structural, optical and dielectric properties of copper selenide were characterized using X-ray diffraction, scanning electron microscopy, and UV-visible spectrophotometry techniques. Also, the lattice parameters, microstrain, grain size, dislocation density, stacking faults, and absorption coefficient spectra as well as the energy band gap and dielectric dispersion are studied in details. In addition, the effects of the gold metal on the optical conductivity spectra and optical conduction parameters are explored through the Drude Lorentz modeling of optical conductivity. The scanning electron microscopy imaging has shown that the two stacked layers of CuSe exhibit needle like grains whose length reaches 1.5 μm. Insertion of gold between layers of CuSe converts the needles to tubes of length of 2.5 μm and width of 220 nm. It was also observed that insertion of Au layers between layers of CuSe increases the strain and dislocation density and decreases the crystallite size leading to a strained structure. Studies of the temperature effects on the structure has shown that increasing the temperature to 473 K increases the grain size and decreases the microstrain and defect density. Optically, the Au nanosandwiching enhanced the light absorbability be more than two times and shrunk the energy bandgap. In addition, an improvement in the dielectric constant in both high frequency and IR range was observed. The optical conductivity analysis also show that the presence of Au improves the optical

conduction and increases the drift mobility making CuSe more appropriate for optoelectronic applications.

List of contents

List of tables

List of Figures

Generalization for the imaginary of Lorentz modeling (black line)

List of Symbols and Abbreviations

α	Absorption coefficient
δ	Dislocation density
β	Full width at high maximum
ε	Dielectric constant
λ	Wave length
ω	Angular frequency
τ	Time relaxation
a,b,c	Crystal unit cell parameters
h,k,l	Miller indices
d	Inter planer spacing in crystal
R	Reflectance
T	Transmittance
E_g	Band gap Energy
XRD	X-ray diffraction
SEM	Scanning electron microscope
$\vec{H}$	Magnetic field
$\vec{E}$	Electric field
$\vec{B}$	Magnetic flux
$\vec{D}$	Electric displacement
$\vec{J}$	Current density

μ   Permeability

Chapter one

Introduction

Copper Selenide -CuSe has attracted attention of researchers and electronic designers, owing to its smart features, different structures and valence states, some unique electrical properties, thermal stability and optical properties. It is used in a number of industrial applications including infrared detection and imaging. Some applications of CuSe include photovoltaic devices, window materials, super ionic conductors, optical filters, electro-optical devices, thermo electric converters, photo electrochemical cells, and photo thermal therapy applications [1].

CuSe exists in different compositions, such as, CuSe, Cu_7Se_4, Cu_5Se_4, Cu_3Se_2, Cu_3Se and $Cu_{2-x}Se$, so it appears in different crystal structures (Monoclinic, hexagonal, tetragonal, and cubic) with different values for bandgaps [1]. For example, bulk and stoichiometric copper selenide (Cu_2Se) is a zero bandgap material with metal-like behavior [2]. However, copper-deficient $Cu_{2-x}Se$ is a p-type semiconductor with direct and indirect bandgap energies in the range of 2.1–2.3 eV and 1.2–1.4 eV, respectively. Its nanocrystalline phase (NCs) have strong localized surface Plasmon resonance absorption which are tunable by their size, shape, and chemical composition [3].

The optical properties of semiconductors including CuSe can be changed by doping; which is the introduction of impurities into a semiconductor crystal. Doping may be p-type or n-type. Due to that we can determine many properties for semiconductors. Doped CuSe has also different optical properties from unhoped CuSe.

Studying the Optical properties is necessary to identify applications for the electronic devices, and to determine the band gap and absorption for the material. Consistently, studying the dielectric dispersion in the CuSe is necessary to determine the active/passive operation modes of the device [2].

As the Au nanosandwiching is certified to have great effect in enhancing the light absorbability of materials. As though we will employ it for the CuSe (CAC-0). Particularly, two layers of CuSe will be sandwiched with Au film of Nano level thickness 25 and 50 nm to form CuSe-Au (25 nm)-CuSe (CAC-25 nm) and CuSe-Au (50 nm)-CuSe (CAC-50 nm) thin films. The structural, optical and photoelectrical as well as the dielectric properties of the sandwiched films will be investigated as function of light energy and as function of temperature to optimize the most appropriate criteria for producing these films in suitable properties for the production of solar cells.

In the following chapter of this thesis, the necessary information that allow comparison of experiments with theoretical considerations is reported. Some important derivations of theoretical equations will be listed. In the third chapter the experiments which were carried out are described. Some of the instruments operation principles are also mentioned. In the fourth chapter the experimental results and the physical interposition of the results is reported in details. The effect of Au layers insertion on the structural and optical properties is discussed. In the final chapter, some of the concluding remarks will be listed.

Chapter Two
Theoretical Background

2.1 X-ray diffraction

X-ray was discovered in 1895 by Wilhelm Conrad Röntgen, and it's a part of electromagnetic spectrum with wavelength in the range of 0.1 Å to 100 Å. X-ray is used in several areas like medical, education, industry, and it help scientists and physicians to determine the nature of the material by studding how the x-ray radiation interact with atoms within the crystal. This technique was used for the first time for identifying the crystalline phases of materials by William Henry Bragg and his son, William Laurence Bragg in 1900. To study and calculate the interplaner space between successive atomic planes, a reflection condition for constructive interference must be met to satisfy Bragg's equation [6]:

$$n\lambda = 2d\sin\theta \tag{2.1}$$

Where n is the order of reflection maximum, λ is the wavelength for x-ray beam, d is the interplaner spacing and θ is the angle of incident beam. Thus, knowledge of the interplaner spacing is necessary to calculate the lattice parameters as appears in the next equations [7]:

$$\frac{1}{d^2} = \frac{\frac{h^2}{a^2}\sin^2\alpha + \frac{k^2}{b^2}\sin^2\beta + \frac{l^2}{c^2}\sin^2\gamma + \frac{2kl}{bc}\cos\alpha + \frac{2hl}{ac}\cos\beta + \frac{2hk}{ab}\cos\gamma}{1 - \cos^2\alpha - \cos^2\beta - \cos^2\gamma + 2\cos\alpha\cos\beta\cos\gamma} \tag{2.2}$$

Where h, k, and l are the miller indices, a, b and c are the lattice constant

If we take the previous equations for cubic crystal, the following conditions must be met:

$\alpha = \beta = \gamma = 90°$ and a= b=c, then, by satisfying the first condition equation (2.2) can be written as

$$\frac{1}{d^2} = \frac{h^2}{a^2} + \frac{k^2}{b^2} + \frac{l^2}{c^2} \qquad \text{(2. 3a)}$$

And by applying the second condition (a= b=c) it can be written as:

$$\frac{1}{d^2} = \frac{h^2+k^2+l^2}{a^2} \qquad \text{(2.3b)}$$

Also, we can apply equation (2.2) on all crystal systems to calculate the expression for interplaner spacing that appears on Table 2.1 for every crystal system:

Table 2.1: The cell constant, angels and inter planer spacing for crystal systems.

Crystal system	Cell constant	Angels	Inter planer spacing
Cubic	$a = b = c$	$\alpha = \beta = \gamma = 90°$	$\dfrac{1}{d^2} = \dfrac{h^2 + k^2 + l^2}{a^2}$
Hexagonal	$a = b \neq c$	$\alpha = \beta = 90°; \gamma = 120°$	$\dfrac{1}{d^2} = \dfrac{4}{3}\left(\dfrac{h^2 + k^2 + hk}{a^2}\right) + \dfrac{l^2}{c^2}$
Trigonal	$a = b \neq c$	$\alpha = \beta = \gamma \neq 90°$	$\dfrac{1}{d^2} = [(h^2 + k^2 + l^2)sin^2\alpha + 2(hk + kl + lh)(cos^2\alpha - \cos\alpha)]\dfrac{1}{a^2(1 - 3cos^2\alpha + 2cos^3\alpha)}$
Tetragonal	$a = b \neq c$	$\alpha = \beta = \gamma = 90°$	$\dfrac{1}{d^2} = \dfrac{h^2 + k^2}{a^2} + \dfrac{l^2}{c^2}$
Orthorhombic	$a \neq b \neq c$	$\alpha = \beta = \gamma = 90°$	$\dfrac{1}{d^2} = \dfrac{h^2}{a^2} + \dfrac{k^2}{b^2} + \dfrac{l^2}{c^2}$
Monoclinic	$a \neq b \neq c$	$\alpha = \beta = 90°; \gamma \neq 90°$	$\dfrac{1}{d^2} = \left(\dfrac{h^2}{a^2} + \dfrac{k^2}{b^2}sin^2\beta - \dfrac{2hl}{ac}cos\beta\right)csc^2\beta$
Triclinic	$a \neq b \neq c$	$\alpha \neq \beta \neq \gamma \neq 90°$	$\dfrac{1}{d^2} = \dfrac{1}{V^2}(h^2b^2c^2sin^2\alpha + k^2a^2c^2sin^2\beta + l^2a^2b^2sin^2\gamma + 2hkabc^2(cos\alpha\,cos\beta - cos\gamma)$ $+ 2kla^2bc(cos\beta cos\gamma - cos\alpha) + 2hlab^2c(cos\gamma cos\alpha - cos\beta))$

Also we can determine the grain size for the crystal by using Scherrer equation which is based in its derivation on the kinematical theory of diffraction [8],

$$\beta cos\theta = \frac{k\lambda}{D} \qquad (2.4)$$

Where β is the full width at half maximum intensity of a peak in radians, k is the shape factor (k = 0.94), θ is the angle at which the peak maxima appear and D is the grain size [9].

2.2 Strain (ε)

Strain measures how much the crystal will be stretched when a force is applied to it, and we can calculated ε depending on the X-ray data that results by using the following equation [10]:

$$\varepsilon = \frac{\beta}{4\tan\theta} \qquad \text{(unit less)} \qquad (2.5)$$

2.3 Dislocation density (δ)

A physical quantity that expresses the number of dislocations intersecting a unit area is the dislocation density δ [11], and it based on values of grain size and strain. We can calculate δ by using the equation [12]:

$$\delta = \frac{15\varepsilon}{a\,D} \quad (\,line/cm^2\,) \qquad (2.6)$$

2.4 Stacking faults (SF %)

Stacking faults (SF) play an important role in describing the dielectric permittivity, and we can calculate it by using X-ray data as the following equation expresses [13]:

$$SF = \frac{2\,\pi^2\beta}{45\sqrt{3}\tan\theta} \qquad (2.7)$$

2.5 Optical absorption coefficient

Optical absorption coefficient is the most important parameter that is used to determine the bandgap energy of a material, we know that if the valance band has many electron and the conduction band contains a lot of empty states, the probability of photon absorption will be high.

The optical absorption coefficient based on the values of transmittance and reflectance measurements as illustrated in the following equations [14]:

$$T = \frac{(1-R)^2 e^{-\alpha d}}{1-R^2 e^{-2\alpha d}} \qquad (2.8)$$

Where R is the reflection coefficient, α is the absorption coefficient and d is the thickness of the sample. If we assume that $R^2 e^{-2\alpha d} \ll 1$, then

$$T = (1 - R)^2 e^{-\alpha d} \qquad (2.9)$$

$$\alpha = -\frac{1}{d} \ln \frac{T}{(1-R)^2} \qquad (2.10)$$

Also, the band gap can be calculated based on the following Tauc's relation:

$$(\alpha E)^n = C\left(E - E_g \right) \qquad (2.11)$$

Where C a constant that is based on the transition probability, n is an index which is theoretically equals to $\frac{1}{2}$ for indirect allowed, 2 for direct allowed, $\frac{1}{3}$ for indirect forbidden and $\frac{2}{3}$ for direct forbidden transitions [15, 16].

2.6 Dielectric function

The dielectric function is important to describe the response of the material to all photons energies, and so, it defines the physical and chemical properties of material that are attached to storage, lost energy and its suitability for a specific application. So, in such experiments we need to determine the complex dielectric function through studying some observations such as transmission and reflection. Also we need to study Maxwell's equations (with assumption that the charge density is zero) to introduce the complex function as the following [17]:

$$\nabla \times \vec{H} - \frac{1}{c}\frac{\partial D}{\partial t} = \frac{4\pi}{c}\vec{J} \qquad (2.12)$$

$$\nabla \times \vec{E} + \frac{1}{c}\frac{\partial \vec{B}}{\partial t} = 0 \qquad (2.13)$$

$$\nabla . \vec{D} = 0 \qquad (2.14)$$

$$\nabla . \vec{B} = 0 \qquad (2.15)$$

Where $\vec{H}$ the magnetic is field, $\vec{E}$ is the electric field, $\vec{B}$ is the magnetic flux $\vec{D}$ is the electric displacement and $\vec{J}$ is the current density.

If we write the constitutive equations as:

$$\vec{D} = \varepsilon\vec{E} \qquad (2.16)$$

$$\vec{B} = \mu\vec{E} \qquad (2.17)$$

$$\vec{J} = \sigma\vec{E} \qquad (2.18)$$

Where ε is the dielectric constant μ is the permeability and σ is the conductivity.

We can get a wave equation for $\vec{E}$ from Maxwell's equations and constitutive equations:

$$\nabla^2\vec{E} = A\frac{\partial^2\vec{E}}{\partial t^2} + B\frac{\partial\vec{E}}{\partial t} \qquad (2.19)$$

Where $A = \frac{\varepsilon\mu}{c^2}$ and $B = \frac{4\pi\sigma\mu}{c^2}$

We will take a sinusoidal solution for the optical field which express as:

$$\vec{E} = \vec{E}_0 e^{i(K.r - \omega t)} \qquad (2.20)$$

Where E is the electric field, ω is the angular frequency

Substitute equation (2.20) in equation (2.19) we obtain the following relation

$$-K^2 = -\frac{\varepsilon \mu \omega^2}{c^2} - \frac{4\pi i \sigma \mu \omega}{c^2} \qquad (2.21)$$

Then $K = \frac{\omega}{c}\sqrt{\mu \, \varepsilon_{complex}}$

Where the complex dielectric function can written as

$$\varepsilon_{complex} = \varepsilon + \frac{4\pi i \sigma}{\omega} = \acute{\varepsilon} + i\acute{\acute{\varepsilon}} \qquad (2.22)$$

Where $\acute{\varepsilon}$ is the real part of permittivity, $\acute{\acute{\varepsilon}}$ is the imaginary part related to absorptive behavior of the material and i is a complex number. Practically, the effective dielectric constant is determined from Fresnel's equation for normal incidence which takes the form [17]:

$$R = \frac{(1-\hat{n})^2 + \hat{k}^2}{(1+\hat{n})^2 + \hat{k}^2} \qquad (2.23)$$

And the dielectric properties for the material are investigated by defining the complex

constant $K = \frac{w}{c} N_{complex}$.

Where $N_{complex} = \hat{n} + i\hat{k} \qquad (2.24)$

Where $\hat{n}$ is the index of refraction and $\hat{k}$ is extinction coefficient $= \frac{\alpha\lambda}{4\pi}$.

Also we can write $N_{complex}$ in the following expression:

$$N_{complex} = \sqrt{\mu\, \varepsilon_{complex}} \qquad (2.25)$$

Where $\varepsilon_{complex} = \varepsilon_1 + i\varepsilon_2$

For non-magnetic materials, we take $\mu = 1$ in equation 2.25 and so:

$$\varepsilon_{complex} = (N_{complex})^2 = (\hat{n} + i\hat{k})^2 \qquad (2.26)$$

So $\varepsilon_{complex} = \hat{n}^2 + \hat{k}^2 + i2\hat{n}\hat{k} \qquad (2.27)$

Compare equation 2.26 with equation 2.27 we get:

$$\varepsilon_1 = \hat{n}^2 - \hat{k}^2 \qquad (2.28)$$

$$\varepsilon_2 = 2\hat{n}\hat{k} \qquad (2.29)$$

2.7 The Drude model

Drude model is used to describe the transport properties of conducting materials, and it's based on the nearly free electron model and on the classical equations of motion for electrons in the optical electric field.

The drift velocity equation of carriers in classical physics is given by

$$m\frac{d\vec{v}}{dt} + \frac{m\vec{v}}{\tau} = e\,\overrightarrow{E_0}\,e^{-i\omega t} \qquad (2.30)$$

Where τ is the relaxation time, and the electrons here undergo a sinusoidal motion as the following

$$\vec{v} = \overrightarrow{v_0}e^{-i\omega t} \qquad (2.31)$$

And then, equation 2.25 become

$$\left(-mi\omega + \frac{m}{\tau}\right)\vec{v_0} = e\vec{E_0} \tag{2.32}$$

Then if we take the current density that is related to the drift velocity and the carrier density n by

$$\vec{j} = ne\vec{v_0} = \sigma\vec{E_0} \tag{2.33}$$

Substitution for the drift velocity $\vec{v_0} = \dfrac{e\vec{E_0}}{\left(\frac{m}{\tau}\right)-im\omega}$ into equations 2.28 introduce the complex

conductivity

$$\sigma = \frac{ne^2\tau}{m(1-i\omega\tau)} \tag{2.34}$$

Where equation 2.29 is the Drude expression for σ.

Drude developed his model to describe the refraction complex index and dielectric constant for metals. So Drude model needes to be modified by adding Lorentz model in order to be used for semiconductors to describe the dielectric function. By that modifying we can get the following expression for dielectric function:

$$\varepsilon(\omega) = 1 - \sum_i^N \frac{\omega_{pei}^2}{(\omega^2+i\omega\gamma_i)} + \sum_i^N \frac{\omega_{pei}^2}{(\omega_{ei}^2-\omega^2)+i\omega\gamma_i} \tag{2.35}$$

Where $\omega_{pe} = \sqrt{\dfrac{4\pi ne^2}{m^*}}$ the electron bounded plasma frequency, n and m* are the free electron density and the effective mass of free electrons, respectively. Equation 2.35 express the Drude-Lorentz model for dielectric functions.

Chapter Three
Experimental Details

3.1 Substrate cleaning

The glass substrates were cleaned using alcohol in order to remove contaminants from the surface. Then, they were shaked by ultrasonic resonator in distilled water at 60 °C for 20 min , after that we flooded the substrate in alcohol before drying prior to deposition. The used glass substrates are shown in figure 3.1.
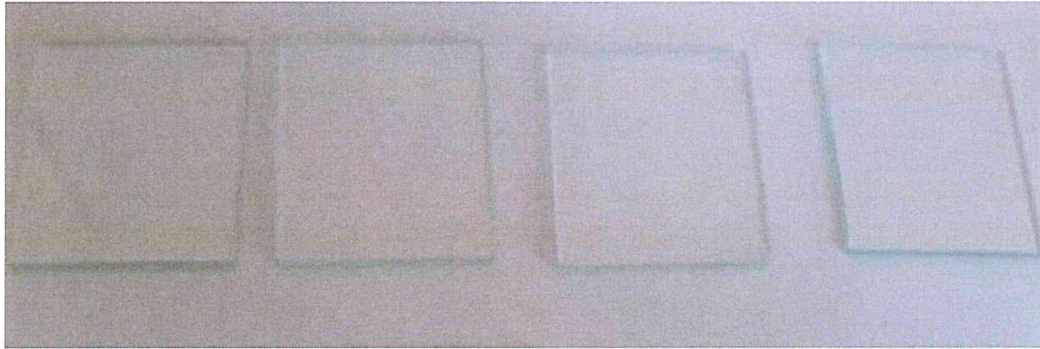
Figure 3.1: Clean glass samples.

3.2 Thin films preparation

CuSe and Au were used as raw materials to prepare CuSe thin films with a thicknesses of 1 μm (CAC-0), CAC-25 nm and CAC-50 nm for layered films, in the first step CuSe films of thickness 500 nm were grown as substrates onto clean glass, then the CuSe substrates were coated with 25 and 50 nm Au. The coating was actualized with ion coater so that the Au particles are accelerated before striking the CuSe substrates. The resulting CuSe/Au-25 nm (CA-25 nm) and CuSe/Au-50 nm (CA-50 nm) were recoated by CuSe to form the proposed layered film. A thickness 0.5 μm and 1 μm of CuSe which are shown in figure 3.2, were evaporated onto glass substrates by physical evaporation technique using VCM-600 thermal vacuum evaporator at a vacuum pressure of 10^{-5}

m bar. The system is shown in figure 3.3.a. The powder of CuSe was placed in a tungsten boat (part of the device, item 1 in figure 3.3.b) after being weighed (0.2 g). Then, the glass and metal substrates were located 20 cm above the source by mounting them onto metal plate (item 2 in figure 3.3b). A manual shutter located above evaporation source was used to avoid the random evaporation during the deposition process (item 3 in figure 3.3.b). Then, accelerated particle technique by ion coater (figure 3.4) have been used in order to deposit 25 nm and 50 nm Au on CuSe films, forming CA-25 nm and CA-50 nm layered films. The film thickness of CuSe layer was measured with the help of STM-2 inficon thickness monitor attached to the evaporator. The monitor works based on quartz crystal can read 3000 reading / second and have a resolution of 0.03 A°.
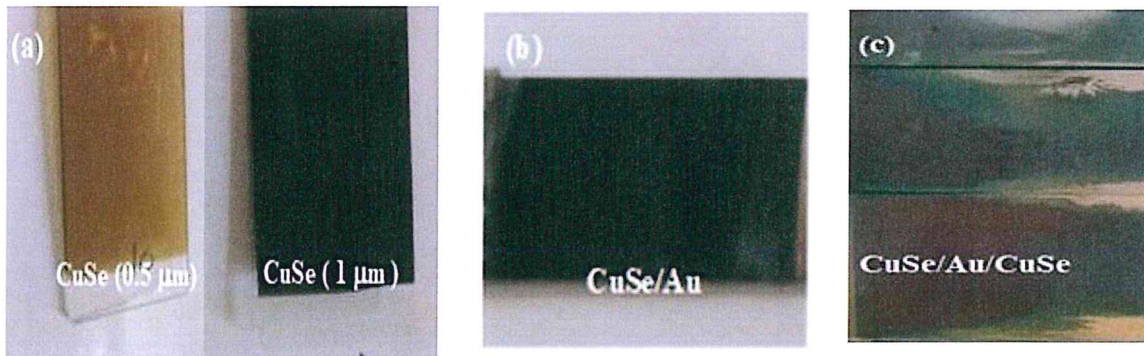
Figure 3.2: (a) CuSe Samples, (b) CuSe/Au sample and (c) CAC samples

Figure 3.3: (a) The VCM-600 thermal evaporator (b) the inside of VCM-600 and (c) the screen of the thickness monitor.
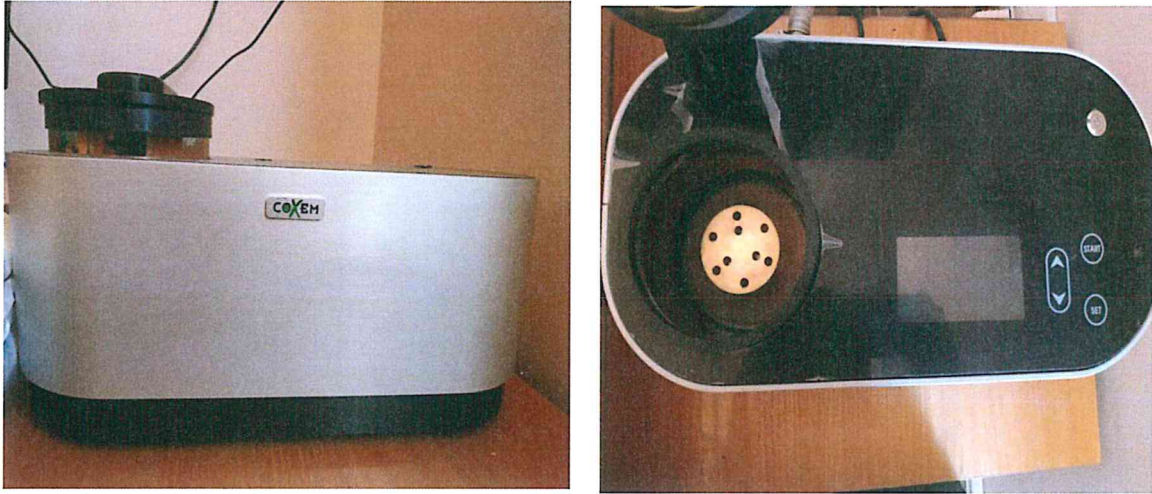
Figure 3.4: Ion Coater used to grow nano sheets of gold

3.3 Thin films analysis

In the following sections we report the methods used to achieve the scientific results. Some of these methods are the hot probe technique to determine the conductivity type, the X-ray diffraction to observe the structure and the optical spectroscopy to explore the band gap and dielectric dispersion in the films.

3.3.1 Hot probe technique

The majority carrier type determines whether the semiconductor material is p-type or n-type. So we use the thermoelectric or hot probe technique as figure 3.5 shows to set the majority carrier type. By this technique there are two probes contact to the surface of the sample, one of these probes (connected to positive terminal of a voltmeter) is heated to a temperature higher than the other side, and the majority carriers at the hot probe have a thermal energy greater than that at the

cold probe, So the majority carrier diffuse away from the hot probe. This introduces a current which flows towards a hot probe in n-type and hence current will pass through voltmeter from positive to negative giving a positive voltage reading. For p-type semiconductor, the current will flow towards cold probe causing a negative reading of the voltmeter as illustrated in figures 3.5 and 3.6. Through this experiment, all prepared film show p-type semiconducting characteristics.
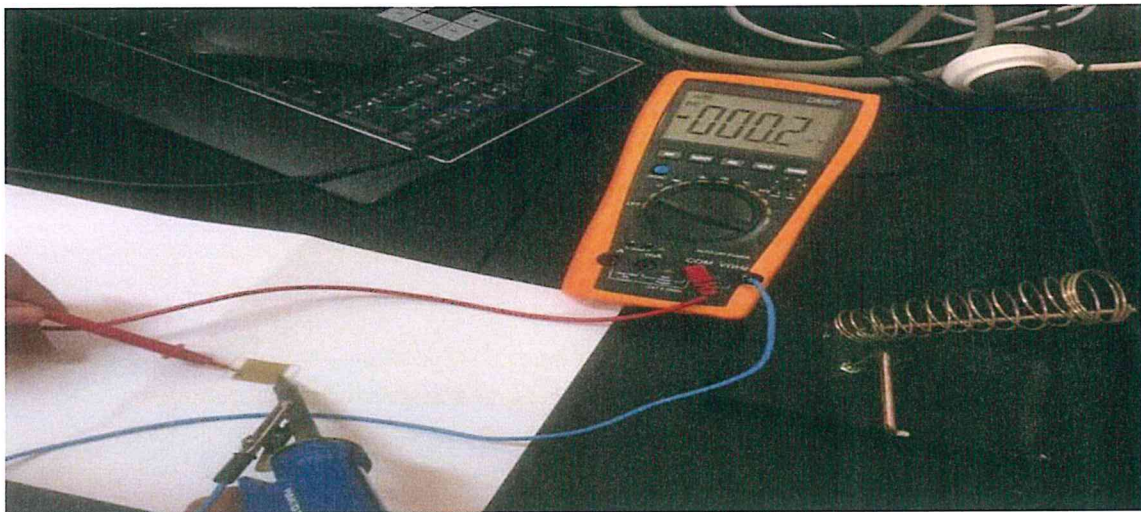
Figure 3.5: Hot probe technique
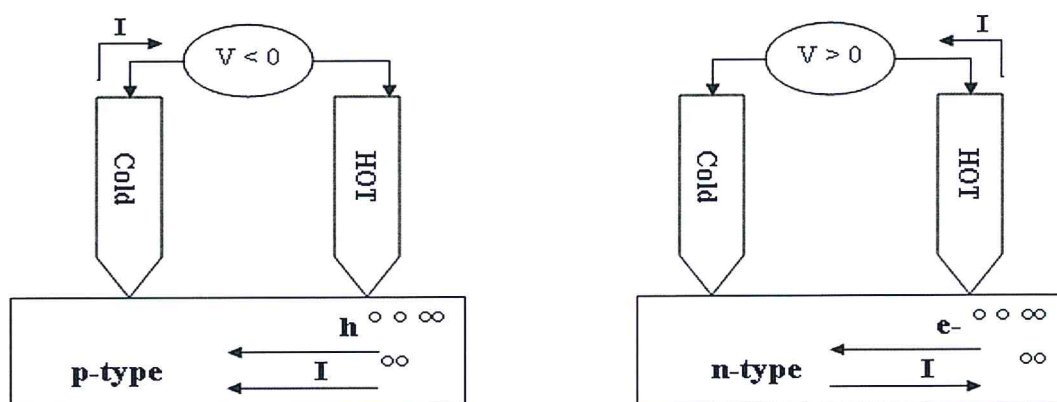
Figure 3.6 Schematic representation of hot probe technique

3.3. 2 X-ray diffraction

X-ray diffraction (XRD) technique is important to study atomic arrangement and structures of crystals. By using Rigaku diffractometer equipped with Kα radiation of a copper anode of average wavelength 1.5405 Å at 40 KV and 15 mA we are able to record the x-ray diffraction patterns for the samples. The x-ray unit is shown in figure 3.7. By this technique we measure the intensity as a function of diffraction angle in order to calculate the lattice parameters for the films which are important to determine the physical properties of materials.

In order to collect the XRD-data we run the generator, the computer device and the X-ray source. Then we open Miniflex Guidance program, and justify the X-ray diffraction for the angle (θ) from 10° to 70°, speed being 1deg /min, and the step is 0.05 in Minflex program and following some steps as appears in chart 3.1 to study the sample properties. Also, for studying the effect of temperature on the structure and morphology of the samples we run the heater in addition to the generator, the computer device and the X-ray source and take the XRD-data every 30 C° by the steps that appear in the chart 3.1.
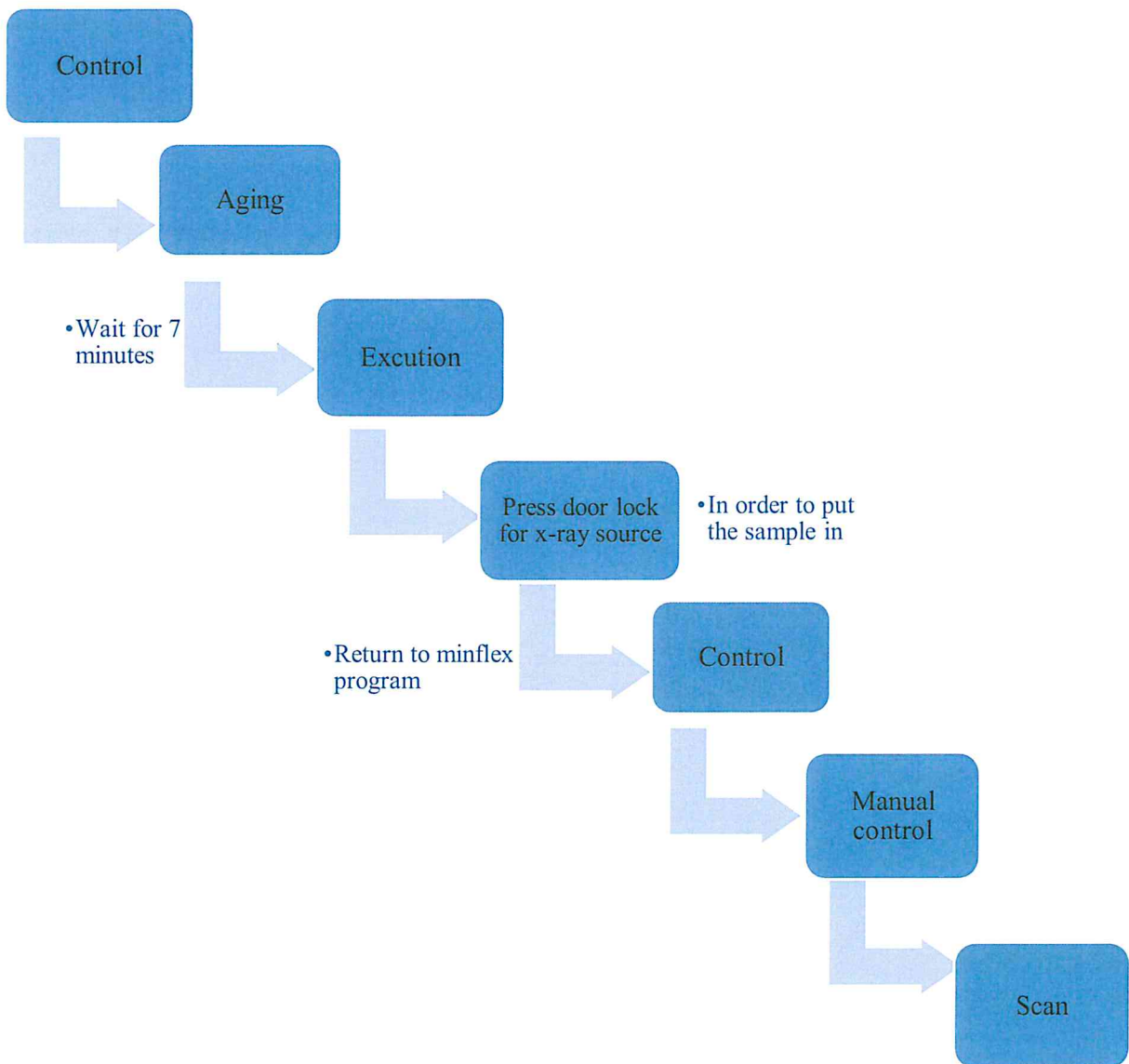
Chart 3.1: X-ray measuring.

Figure 3.7: (a) Rigaku Diffractometer and (b) Miniflex program (c) The heater beside Rigaku Diffractometer.

3.3.3 Scanning electron microscope (SEM)

SEM offers high-resolution picture about the size of particles, so, it's necessary to study the surface topography of the material. The schematic diagram of SEM appears in Figure 3.8 [18] which shows that the column of the SEM consists of electron source which ejects and accelerate the electrons to have an energy with a range of 1-30 K eV. It consists of condenser and objective lens, two scan coils and electron detector.
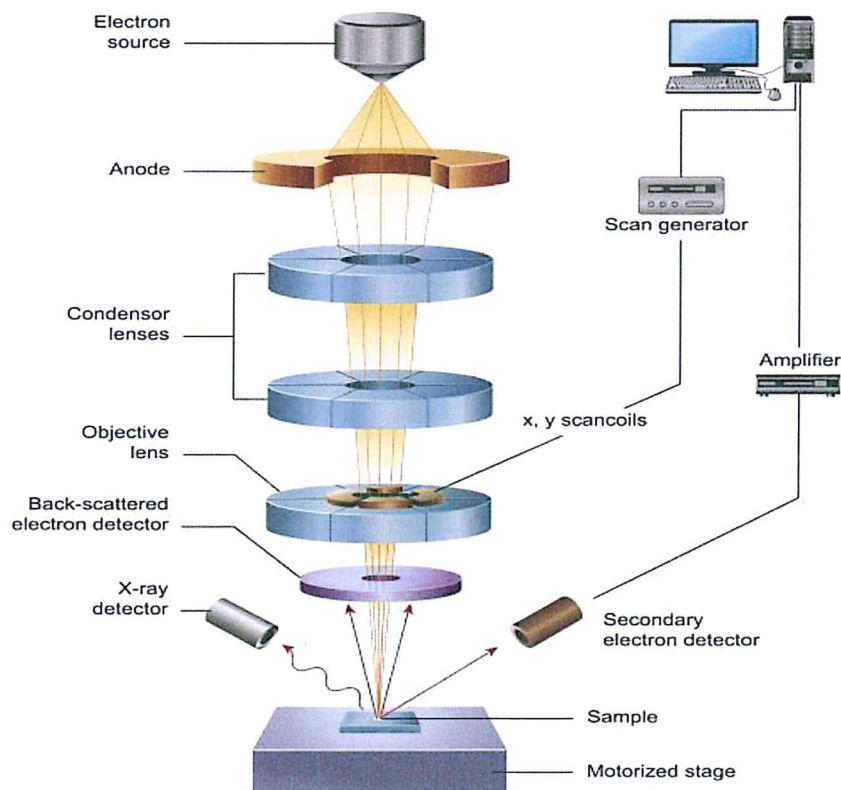
Figure 3.8: A schematic diagram of scanning electron microscope.

In this technique (studying the samples by the SEM) the image formation is based on signals produced by electron beam that is aligned by scan coils and interact with specimen surface (elastic and inelastic interactions).
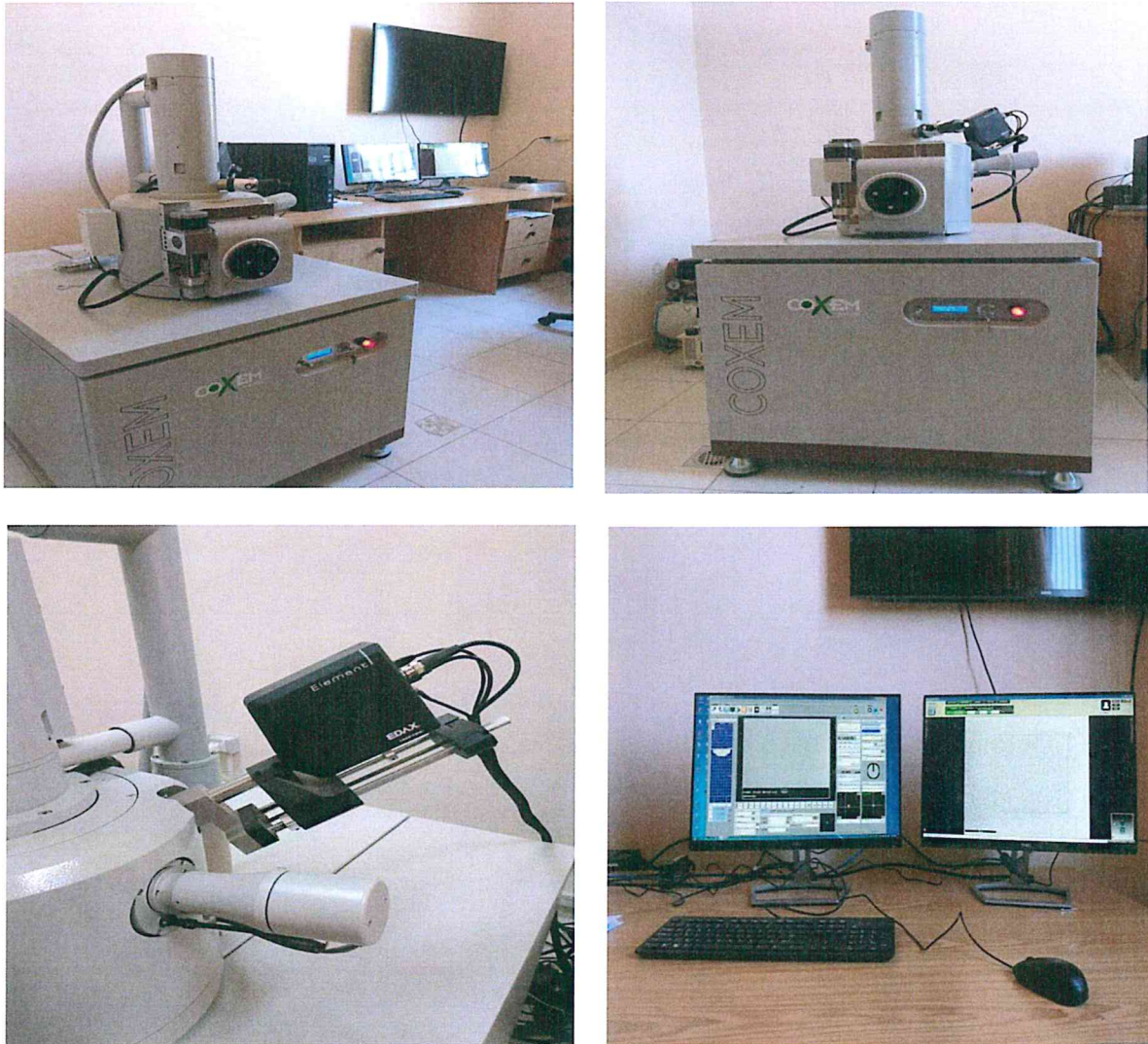
Figure 3.9 Scanning electron microscope (SEM).

3.3.4 Optical measurements

Optical transmittance and reflectance offer important tool to determine the material absorbability, dielectric dispersion and optical band gap. These parameters are measured in the incident light wavelength range of 300–1100 nm by using a thermo- scientific Evolution 300 spectrophotometer which is equipped with VeeMax II spectrophotometer that is shown in figure 3.10. The measurements are actullized by the reflectometer at about normal incidence (15°). The data here were collected by VISION software.
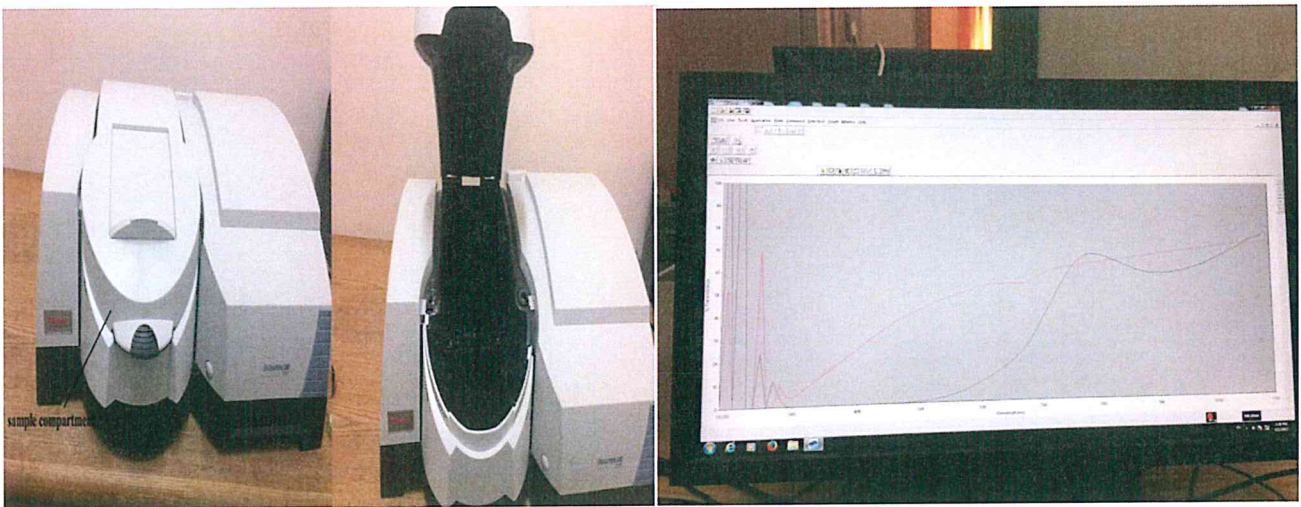
Figure 3.10: The VeeMax II spectrophotometer.

Chapter Four
Results and discussion

4.2 Scanning Electron Microscopy

The SEM images for the studied CAC-0 (CuSe film), CAC-25   (CuSe/Au-25 nm/CuSe) and CAC-50 (CuSe/Au-50 nm /CuSe) samples are shown in Fig. 4.1 (a), (b) and (c), respectively. While the insets of the figures show enlargements of 10k, the main figures display enlargements of 30k for the as grown samples and 50k for the samples sandwiched with Au slabs. It is clear from the inset of Fig. 4.1 (a), that the CuSe films are composed of needle like grains, they are mostly randomly distributed. The closer look with 50k enlargements show that   these grains are of 1.4 μm length and of average width of 214 nm. When the CuSe films were sandwiched with Au layer of thickness of 25 nm, as can be seen from the inset of Fig 4.1 (b), most of the needle like grains disappeared and the remaining grains exhibited length and widths of 600 nm and ~120 nm, respectively. Further increase in the content of Au to 50 nm, enriched the number of needles (inset Fig. 4.1 (C) and increased the length to 2.3 μm and width to 220 nm. As the length to width ratio exceeds 10 times, it is possible to think that those needles converts to nanotubes.
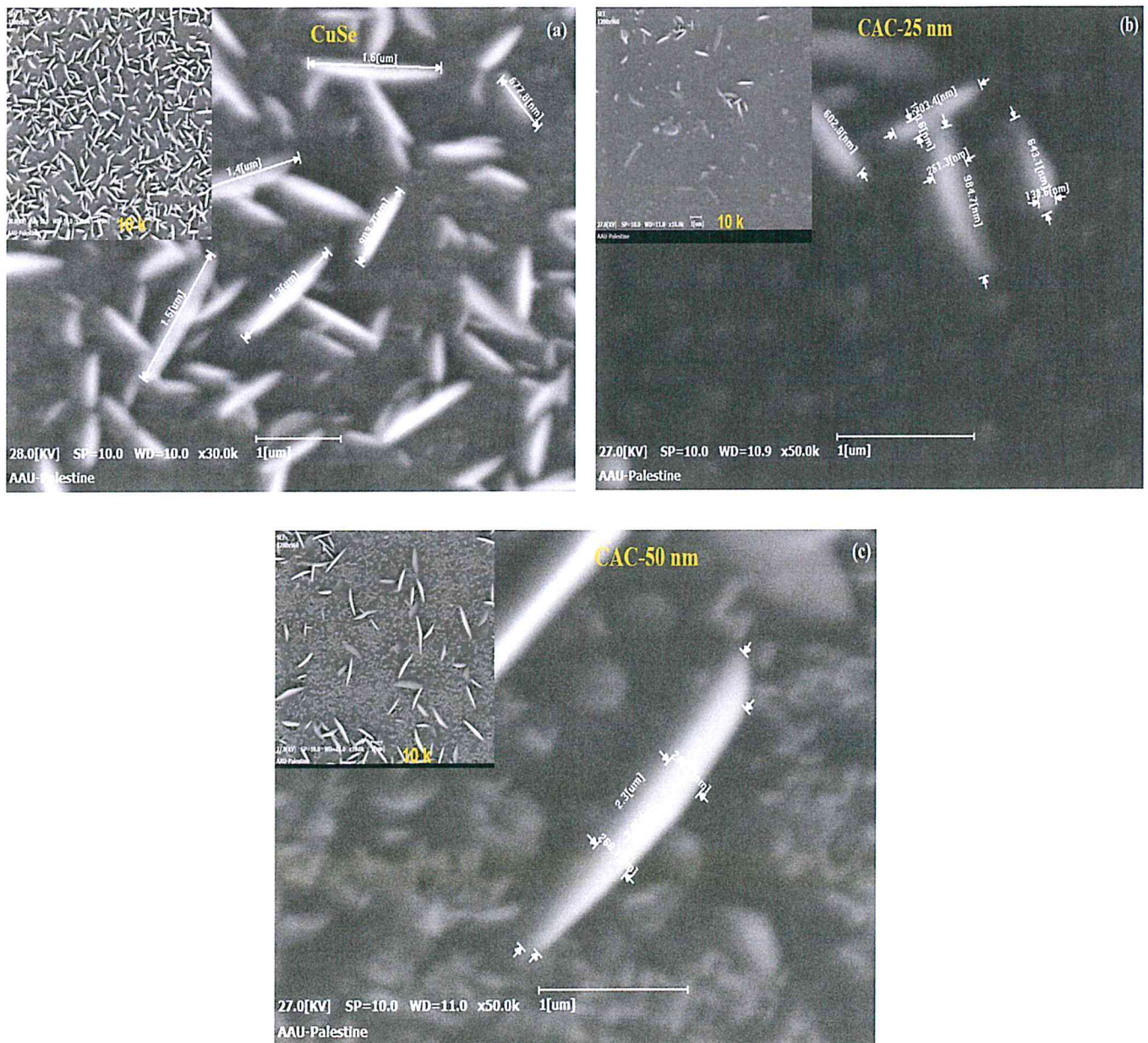
Figure 4.1: The SEM images for (a) CuSe, (b) CuSe/Au-25 nm/CuSe and (c) CuSe/Au-50 nm/CuSe.

On the other hand, the energy dispersive X-ray spectroscopy measurements for the samples under study, which are demonstrated in Fig. 4.2 , have shown that the films are composed of CuSe in addition to glass (SiO_2:MgO:Na_2O:CaO) and Au. In the energy dispersive X-ray spectroscopy measurements for CuSe sample we can see Au atoms, that's because we coat the samples with gold during the experiment to prevent electron cintamination. Also, it is clear from the spectra that the content of Au increases as the slab thickness increase. The atomic content of CuSe in the absence and presence of Au is shown in Table 4.1. One may read from the table, that the CuSe samples contains excess Cu atoms. Insertion of Au into the structure of CuSe, initially increased the content of Cu over that of Se, then it decreases making the Cu/Se ratio closer to the proposed stoichiometric ratio. It is believed that irregular distribution of grains in the films is due to the excess Cu content [19]. This fact is also confirmed when one compare inset of Fig.4.2 (b) with inset of (c). The less the Cu content the more crowded the grains the larger their lengths. It is also reported that excess copper may force formation of Cu_2Se as secondary phase in the structure of the films [20] which may limit the performance of the films through photovoltaic applications. Thus, when Au slab thickness reaches 50 nm, the Cu content significantly decreases and much better performance may be expected.
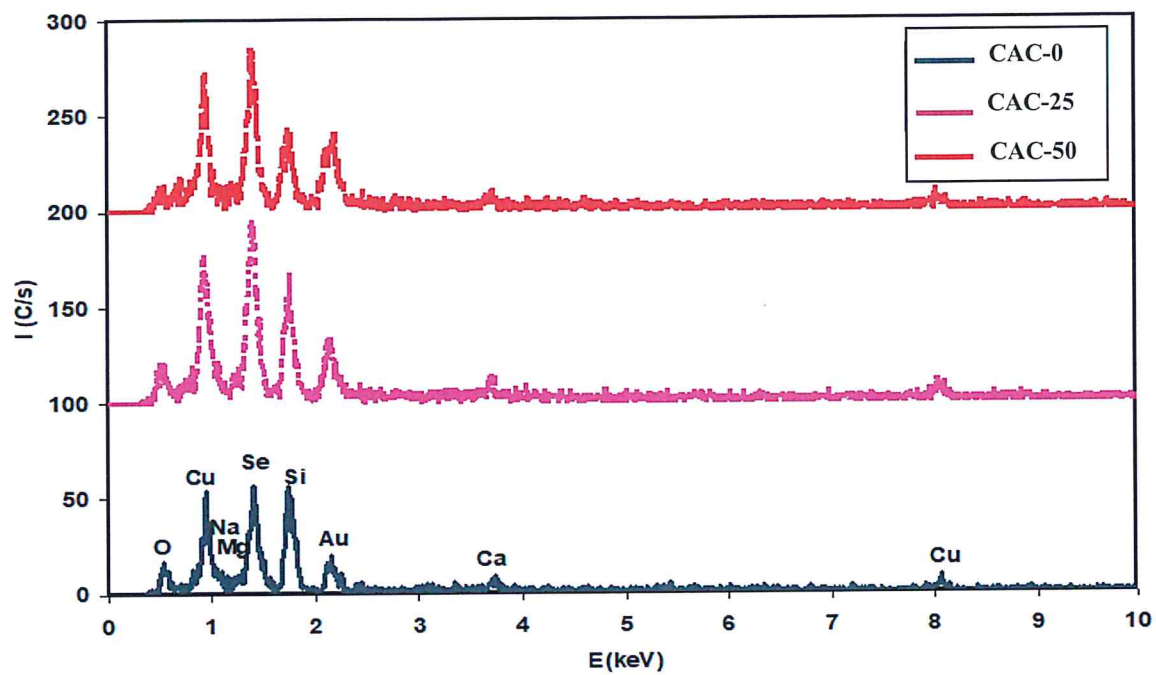
Figure 4.2: Dispersive X-ray spectroscopy measurements for the samples during SEM study.

Table 4:1 The atomic content of CuSe in the absence and presence of Au.

Sample	Cu at. %	Se at. %	Cu/Se
CuSe	52.81	47.19	1.119
CAC-25	53.48	46.52	1.150
CAC-50	51.43	48.57	1.059

4.2 Structural Analysis

The XRD for CuSe thin films of thicknesses of 0.5 μm that are deposited onto glass substrates by thermal evaporation technique are shown in Fig 4.3.The patterns were recorded at varying diffraction angle (2θ) in the range of 10 to 70°.Two types of samples are presented. Namely, those which are pure and the other which are sandwiched with Au nanosheets (CAC-25 nm and CAC-50 nm).

Based on the shown XRD patterns it is clear that CuSe exhibit main peak at 2θ=28.45° with intensity of I=1633 a.u and other minor peaks are detected at 2θ=26.75, 31.4, and at 45.85° The XRD data for glass/CuSe films were analyzed by "TREOR 92" software packages to investigate the polycrystalline nature of CuSe. The analyses reveal that CuSe films are of hexagonal structure with plane orientation in the (102) direction.
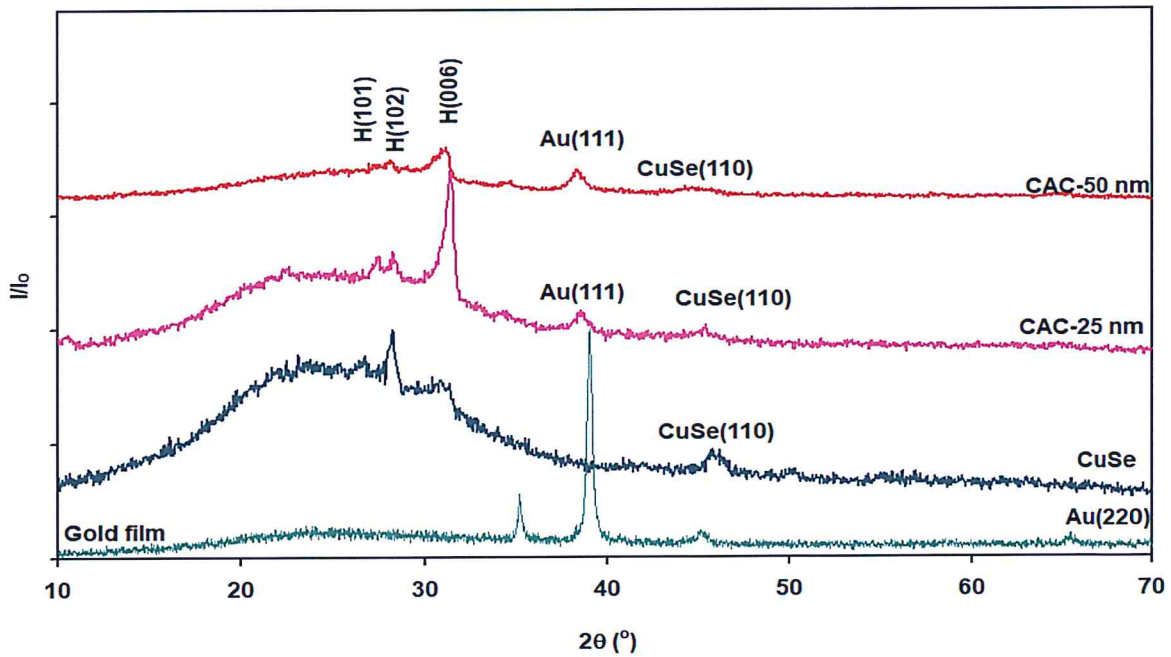
Figure 4.3:X-ray diffraction patterns for CuSe and CAC-25 nm and CAC-50 nm nanosheets.

Since the peaks of the as grown CuSe are not sufficiently sharp, the analysis were based on literature data which report hexagonal phases of CuSe as a most appropriate phase being observed at these angles. In accordance with the hexagonal structural analysis, the lattice constants which are estimated using equation (2) are   a= 3.93 and c=17.04 A˚ .The values are consistent with those reported in literature as a = 3.96 and c=17.23 A° [21].On the other hand, the impact of gold nano layer on the films structure is also investigated. The nanosandwiching of 25 nm thick Au layer between two layers of CuSe caused the appearance of the most intensive peak at 31.4° and also the intensity for (220) and (102) peaks decrease, hence there is a change in the preferential orientation. Repeating the solution for the new XRD patterns, they have shown that the hexagonal phase is still best oriented in the (006) direction. The calculated lattice parameters for this hexagonal cell are a= 3.922 and c= 17.0786 A˚.

As though, and in order to visualize the structural stability upon nano sandwiching, the crystallite size, the micro strain, the defect density and stacking faults are calculated from the peak broadening of the most intensive peak in accordance with equations (2.4), (2.5), (2.6) and (2.7), respectively. The crystallite size and strain for CuSe, CAC-25 nm and CAC-50 nm which were calculated using modified Scherrer equation are shown in Table 4.2. The micro strain (ε), dislocation density (δ) and stacking faults percentages (SF %) increases and the crystallite size (D) decreases as Au layer thickness increases from 0 nm to 50 nm. Study of these parameters in materials is important as it gives indication about the mechanical properties, such as elasticity, hardness and ductility etc. For example, smaller crystallite sizes of material make it weekly structured.

Table 4.2: Structural parameters of CuSe and CAC Nano sandwiches.

Parameters	CuSe	CAC-25 nm	CAC-50 nm
2θ (^{o})	28.25	31.25	31.25
I (a.u)	1916	2365	3657
a (A^o)	3.922	3.930	3.927
c (A^o)	17.07	17.04	17.1
D (nm)	57.0	19.0	17.0
ε x10^{-3}	2.60	6.90	7.74
δx10^{11} (line/cm^2)	1.7	14.1	16.0
SF%	0.18	0.37	0.41

It is clear from Table 4.2 that the Au nano sandwiching strongly alters the crystallization process. This can be understood from the increased intensity and increased broadening of X-rays. In addition, the presence of Au of thickness of 25 and 50 nm in the CuSe structure increase the lattice constant along the a-axis. These changes are ascribed to the lattice mismatch between Au and CuSe [22,23] .Since Au is face centered cubic with lattice parameters of 4.07 A^o, the lattice mismatches between CuSe and Au along the a- c-axes are 3.77% and 76.5%, respectively. Large lattice mismatches causes high interfacial energies [22] which lead to increase in the strain and dislocations. [23]

As shown in Table 4.2, large defect densities are generated upon insertion of 50 nm thick Au layer. This behavior is attributed to the bonding mechanism in CuSe that depends on the system internal

energy. Recalling that the bond length of Au-Se being 2.38 Å [24] is shorter than that of Cu-Se which is 2.49 Å [25], the Au-Se formation weaken the bonding in CuSe.

In addition, as the ionic radius of Au being 1.37 Å [26] is larger that of Cu^{+2} (0.73 Å) [27], Au can replace interstitial positions in CuSe. The non-symmetric substitutions (interstitial) causes large stress values that increases the interface energy [28].

Following the already published work of Qasrawi about temperature effects on structural properties of CuSe, the X-ray scattering data were also collected for CAC-25 nm and CAC-50 nm at different temperatures as shown in figure 4.4 and 4.5, respectively. It's clear that the peak has become narrower and sharper with increasing temperature and shifted to left when the temperature exceeds 383 K (illustrated in the insets of Figure 4.4 and 4.5).
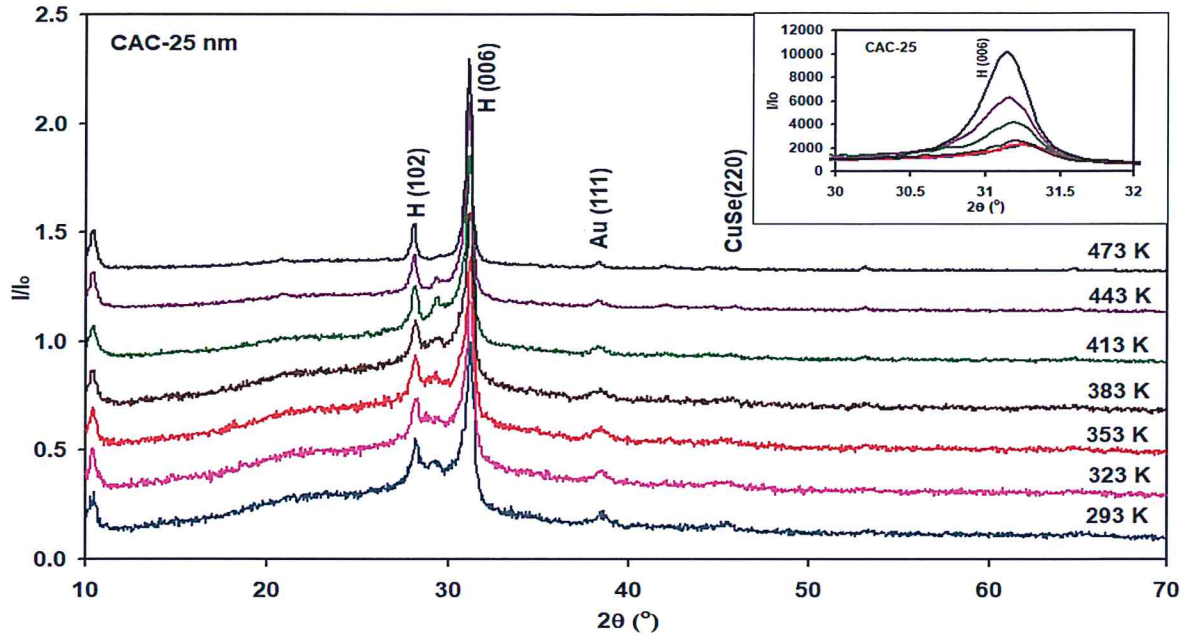
Figure 4.4: XRD pattern for CAC-25 sandwiched with Au nanosheets with annealing.
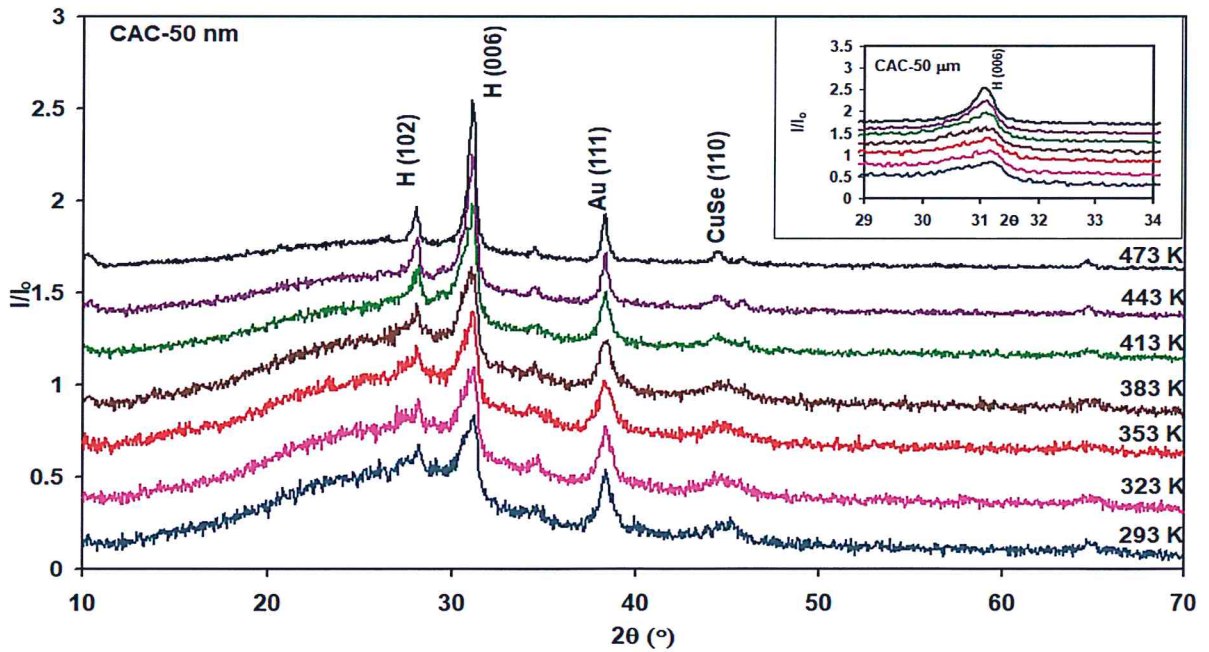
Figure 4.5: XRD pattern for CAC-50 nm sandwiched with Au nanosheets with temperature.

Table 4.3: The structural parameters of CAC-25nm and CAC-50nm at different temperature

Spectrum	CAC-25nm						CAC-50nm				
Temperature (K°)	$2\theta(°)$	Intensity(c/s)	B (rad)	D(nm)	$\varepsilon*10^{-3}$	2θ (°)	Intensity(c/s)	B (rad)	D(nm)	$\varepsilon*10^{-3}$
293	31.2	2365	0.0078	19	6.90	31.2	1061	0.0086	17	7.74
323	31.2	2274	0.0072	20	6.40	31.1	1093	0.015	9	13.4
353	31.25	2337	0.0076	19	6.79	31.5	1120	0.009	16	7.90
383	31.2	2564	0.0082	18	7.34	31.0	1159	0.016	9	14.4
413	31.2	4143	0.0071	20	6.35	31.0	1601	0.012	12	10.8
443	31.15	6358	0.0066	22	5.91	31.0	2115	0.012	12	10.8
473	31.15	10184	0.0059	24	5.29	31.0	1134	0.006	23	5.40

As it is evident from the XRD patterns figure 4.4 for CAC-25 nm and figure for CAC-50 nm, there is an enhancement in crystallization process as the temperature rises .Namely, the grain size increases as the temperature increases to sufficiently high temperatures (above 413) K [29] .As an advantage of these enhancements and as expected by Oswald [30], the larger grains grow bigger at the expense of smaller grains upon heat treatment. Larger grains reduces the number of scattered conducting electrons at grain boundaries which in turn lowers the resistivity [30].

As also illustrated in Table 4.3 during the heating process, the structural parameters doesn't follow systematic behavior. However, accountable difference may be seen when room temperature values are compared to the value obtained at 473 K. Particularly, the intensity of the XRD increases by more than four times, the crystallite size increases by 33% and the micro strain decreased by 23% .It's also observable from the table that increasing the thickness of the Au layer from 25 to 50 nm doesn't play significant role on the temperature effect on the structural parameters.

It is also readable from figure 4.6 (a) and (b) which show the XRD patterns for the samples after cooling that the enhancements in the crystallization processes are permanent. The samples did not return to its initial position before heating. The calculated lattice parameters, grain size, microstrains and defect density values before heating and after cooling are compared in Table 4.4.

As seen from the table which compares the structural parameters of the samples before heating and after cooling, the shape of the unit cell is changed and the intensity of the main peak is increased. Accordingly, the grain size increased from 19 to 26 nm. This enhancement in the crystal structure is accompanied with decrease in the micro strain and defect density and a decrease in the percentage of the faulty stached layers.

The result indicates that the heating processes enhanced crystallinity of the films significantly. The role of the Au thickness on the enhancement of the crystallinity is also evident from the differences in the values of the structural parameters for both samples. Namely , while the insertion of 25 nm thick layer increased the crystallite size and decreased both of the defect density and micro strain by 36.8% ,45.3% and 32.5% respectively, the 50 nm thick Au layer changed the parameters by 47.1% ,50.6% and 33.3% , respectively.

Table 4.4: The structural parameters of CAC-25nm and CAC-50nm before heating and after cooling

Parameters	25 nm							50 nm						
	2θ	I	$Bx10^{-3}$	D	$\varepsilon x10^{-3}$	δ (x10^{11} line/cm^2)	SF%	2θ	I	$Bx10^{-3}$	D	ε	δ (x10^{11} line/cm^2)	SF%
Before heating	31.25	2365	6.1	19	6.9	14.1	0.37	31.2	1042	8.9	17	7.74	16	0.41
After cooling	31.25	12254	6.1	25	5.5	8.3	0.41	31.2	3639	5.2	29	4.6	6.1	0.35
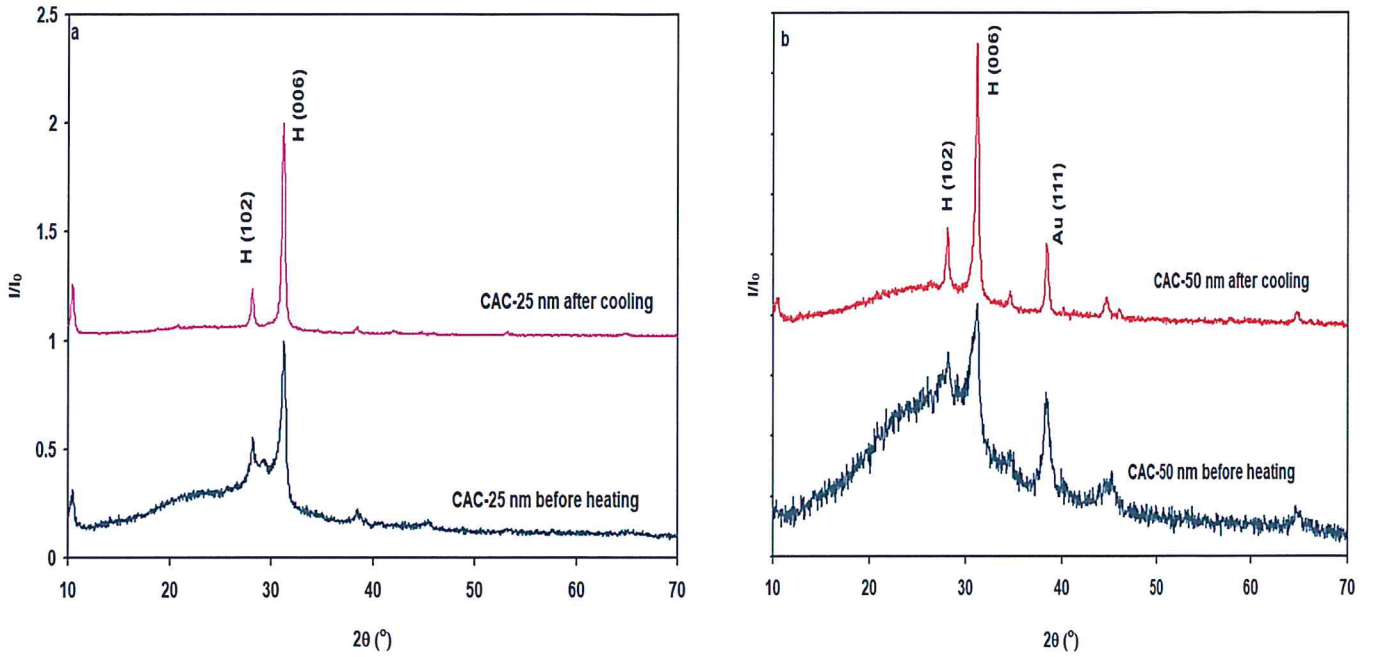
Figure 4.6: XRD pattern for (a) CAC-25 nm and (b) CAC sandwitched with Au nanosheets before heating and after cooling.

This behavior most probably resulted from the better homogenous distribution of heat through the CAC-50 samples due to the availability of more Au atoms (high thermal conductivity) in the thicker samples. In general, heat assisted grain growth which was also observed in many crystalline materials [31], is ascribed to the crystallization and recovery processes .During heating, the small size crystallites are unable to absorb the internal thermal energy, thus during the nucleation process small crystallites that are closer to each other melt forming larger grains. Because the larger crystallite means more oriented planes. The intensity of XRD increases and the strain decreases owing to misaligned planes [32] that caused the strain.

4.2 Optical analysis

The experimental investigation and results for transmittance (T) and reflectance (R) spectra that are obtained using UV-VIS spectrophotometer for CuSe and Au sandwiched CuSe films are displaced in Figure 4.7 and 4.8, respectively. These data were measured in the incident light wavelength range of 300-1100 nm.
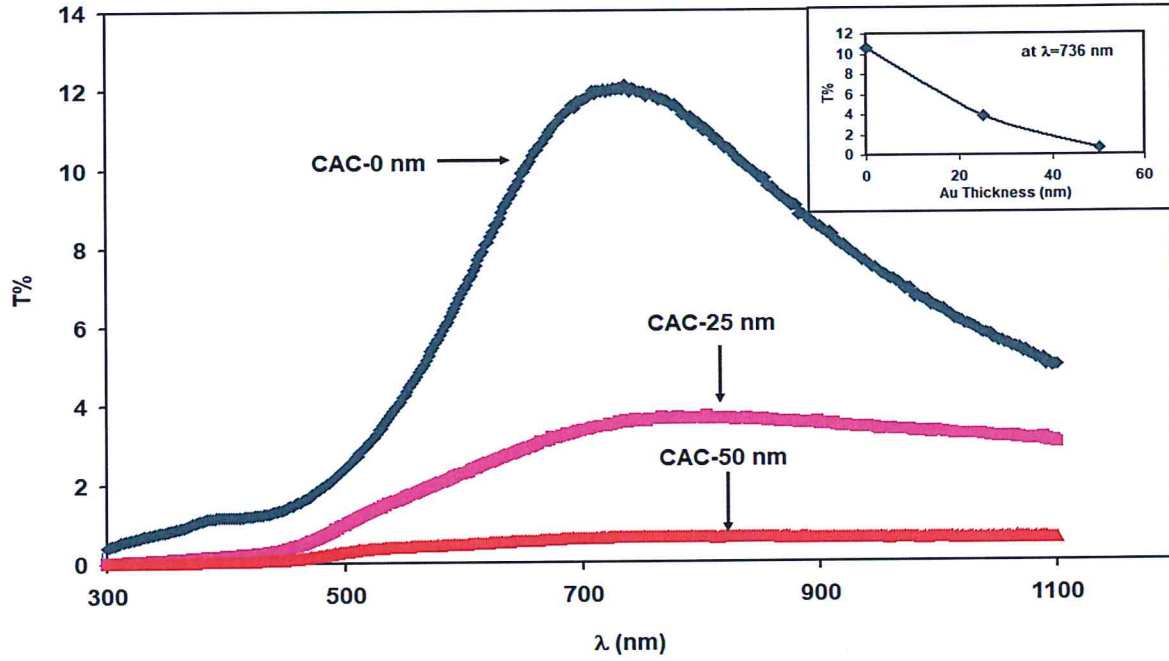
Figure 4.7: The transmittance spectra for CuSe, CAC-25 nm, and CAC-50 nm interfaces, respectively in the range of 300-1100 nm.

The transmittance of CuSe increased with increasing wavelength until the incident photon energy reaches value ~736 nm as shown in Figure 4.7. It then , begins to decrease with increasing λ .In the visible region of light higher transmittance values are observed so, CuSe appears to be more transparent in that region .On the other hand, T spectra for CAC-25nm increases as λ increases to the same value of light wavelength (736 nm). However, for larger λ values, it tends to remain

constant in contrary to the behavior of T spectra in the same region for pure CuSe. In addition

CAC-50 nm samples show the same trend of variation with less values of T indicating that the

samples become weakly transparent. Particularly, as illustrated in the inset of figure 4.5 at λ value

of 700 nm the transmittance decreases as the thickness of Au layer increases.
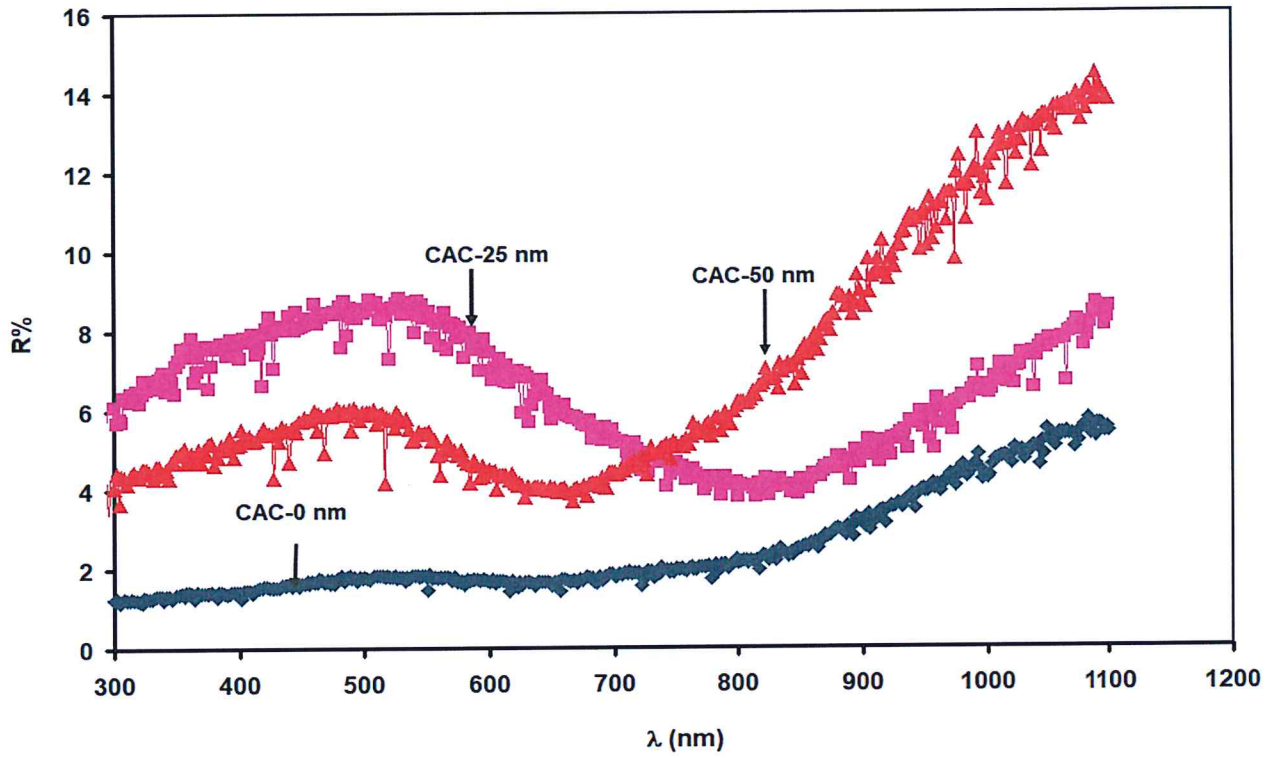
Figure 4.8: Reflectance coefficient for CuSe and CAC-25 nm and CAC-50 nm with incident photon wave length.

On the other hand, the R spectra which appears in Fig 4.8 indicates that the reflectance increases

with increasing λ, however for CAC-25 nm, R increases as λ increases up to a value of 528 nm ,

thereafter, it decreases until the value of 812 nm, and finally re-increase linearly. For CAC-50 nm,

R increases with increasing λ until it reaches 508 nm where R starts decreasing approaching   a

value of 3.9% at 664 nm. Then it return to increase linearly. The reflectance values of the CAC-25 nm samples are less than those of CAC-50nm above ~740 nm, meaning that R% increases with increasing Au thickness near the infrared region, where it decreases in the visible region.

The transmittance and reflectance were used to determine absorption coefficient (α) spectra using eqn. (2.10). The absorption coefficient spectra is shown in Figure 4.9. The Figure show that α spectra of CuSe start decreasing with increasing incident photon energy in the region 1.12 - 1.74 eV then it increases with increasing incident photon energy. For CAC-25, α decreases with decreasing energy till the energy of value 1.68 eV is reached. After that, it increases with increasing energy. Unlike that of CAC-25, α for CAC-50 nm always decreases with decreasing E. The strong absorption in CuSe, CAC-25 nm and CAC-50 nm dominates in the ranges (1.7-2.7 eV), (2.2-2.8eV) and (2.3-2.8eV), respectively.
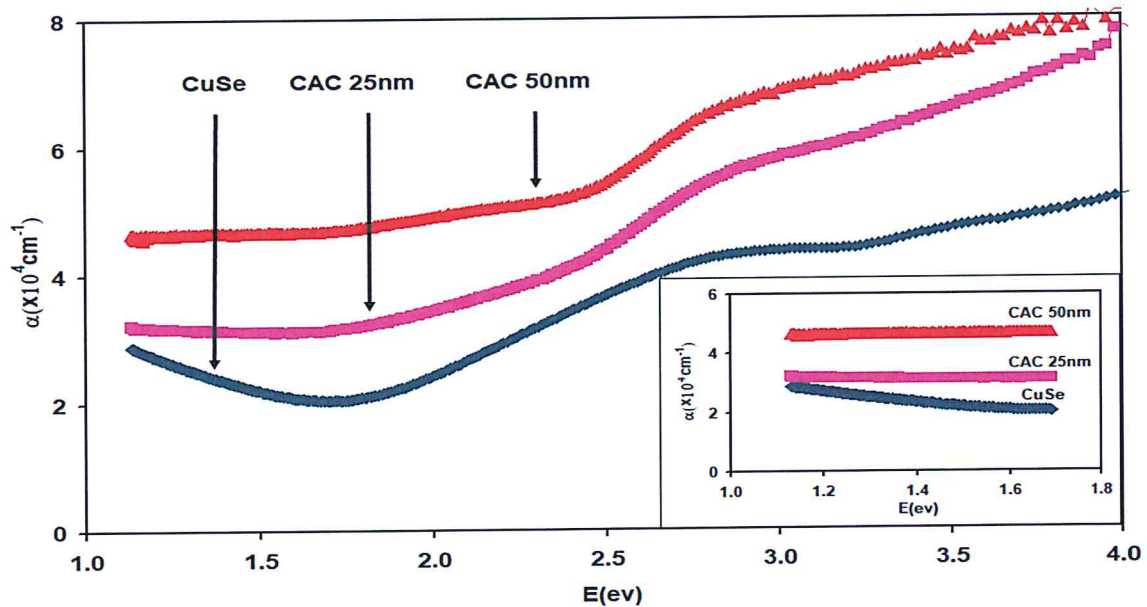
Figure 4.9: The absorption coefficient spectra for CuSe, CAC-25 nm and CAC-50 nm.

In addition, as seen from Figure 4.9, the absorption coefficient increases as the thickness of Au layer increases, indicating that the nanosandwiching of gold between two layers of CuSe enhances the light absorbability in CuSe. The ratio α of light spectra in the presence of Au ($R_\alpha = (\alpha_{CAC}/\alpha_{CuSe})$) is calculated and shown in Figure 4.10 .As seen from the figure, Rα is always larger than a unit and exhibit maxima at 1.68 and at 1.74 eV for CAC-25 and CAC-50 samples, respectively. The maxima Rα value of 2.3 correspond to CuSe sandwiched with 50 nm Au. The enhanced light absorbability is assigned to the quantum confinement achieved by the Au/CuSe interfacing. The work function of p-type CuSe about 4.17 eV which is less than the work function of Au (5.34 eV) [33, 34], indicating the Ohmic nature of metal- semiconductor interaction. As a result no band bending is expected. However, the increased defect density at the surface upon Au insertion could increase the trapping and recombination centers which also could account for the increased absorbability.

Figure 4.10: Rα = ($\alpha_{CAC}/\alpha_{CuSe}$) for CAC-25 and CAC-50 nm.

It worth noting that the increasing trend of variation of α with decreasing incident photon energy in the low range of energy is an 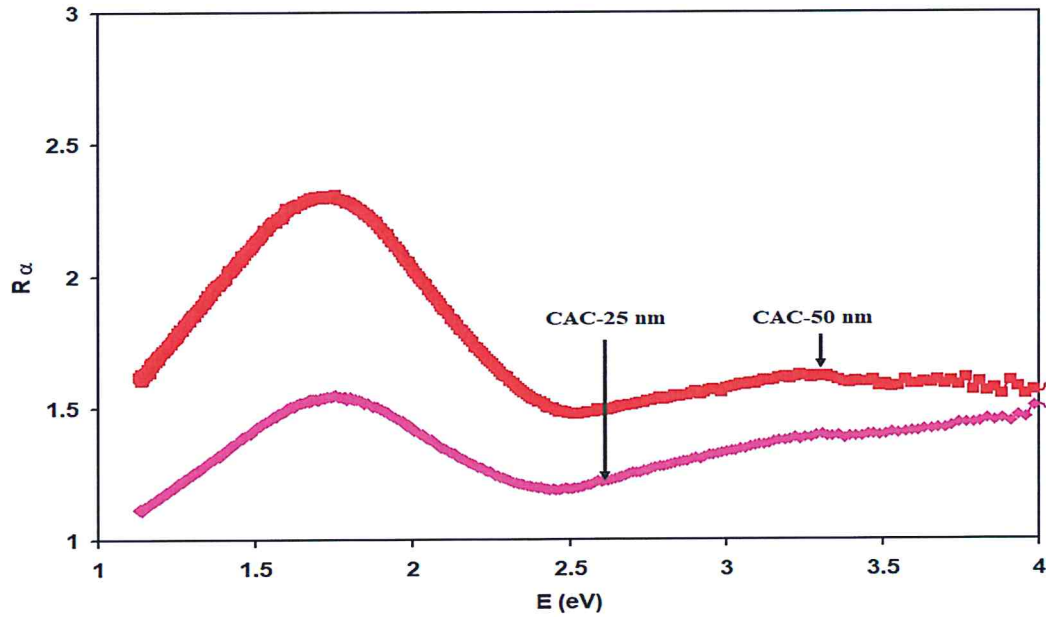indication of the domination of the free carrier absorption mechanism in the pure and CAC-25 samples sandwiched with 25 nm Au. The free carrier absorption mechanism in the IR region was previously [35] observed for ZnO and was assigned to the carrier movement affected by phonon scattering arising from the energy to lattice when irradiated by IR light [36]. As the interfacing between p-type CuSe and Au layer represent Ohmic type, holes flow from CuSe to Au layer. Thus, with increasing metal thickness (CAC-50 nm) and owing to the availability of more electrons at the metal surface no free holes remain in the semiconductor to actualize the free carrier absorption and the mechanism disappears.

The optical band gap of the CuSe, CAC-25nm and CAC-50nm thin films were determined using Tauc's relation, $(\alpha E)^2 = A * (E - E_g)$ by extrapolating the linear part of the Tauc's plot of $(\alpha E)^2$ vs E curve to the E-axis as shown in Figure 4.11 (a), the energy gap were determined to be 2.57 eV for CuSe, 2.55 eV for CAC-25nm, and (2.12 eV) as Au layer increase for CAC-50 nm, so that increasing the thickness of the gold layer shrinks the optical energy band gap [37]. On the other hand, as demonstrated in Figure 4.11 (b), heating the samples at different temperatures caused better recrystallization process .Such process increases the band gap for the two samples as its appears in Figure 4.11 (b) .

The shrinkage in the energy band gap and the formation of interbands in the band gap of CuSe may be assigned to the orbital overlapping between Au atoms and CuSe. The electronic configuration of Au being [Xe] $4f^{14}$ $5d^{10}$ $6s^1$ [38] is at higher orbitals than Cu which have the electronic configuration [Ar] $3d^{10}$ $4s^1$. Au $4f^{14}$ $5d^{10}$ $6s^1$ orbitals can reach the conduction band of CuSe leading to crowding in the density of states and as a result it lowers the band gap. In addition,

as the band length of Au –Se is shorter than that of Cu-Se, at the interface region between Au and CuSe, the possible formation of Au –Se layers creates energy bands that may behave as interbands in the structure of band gap of CuSe [39].
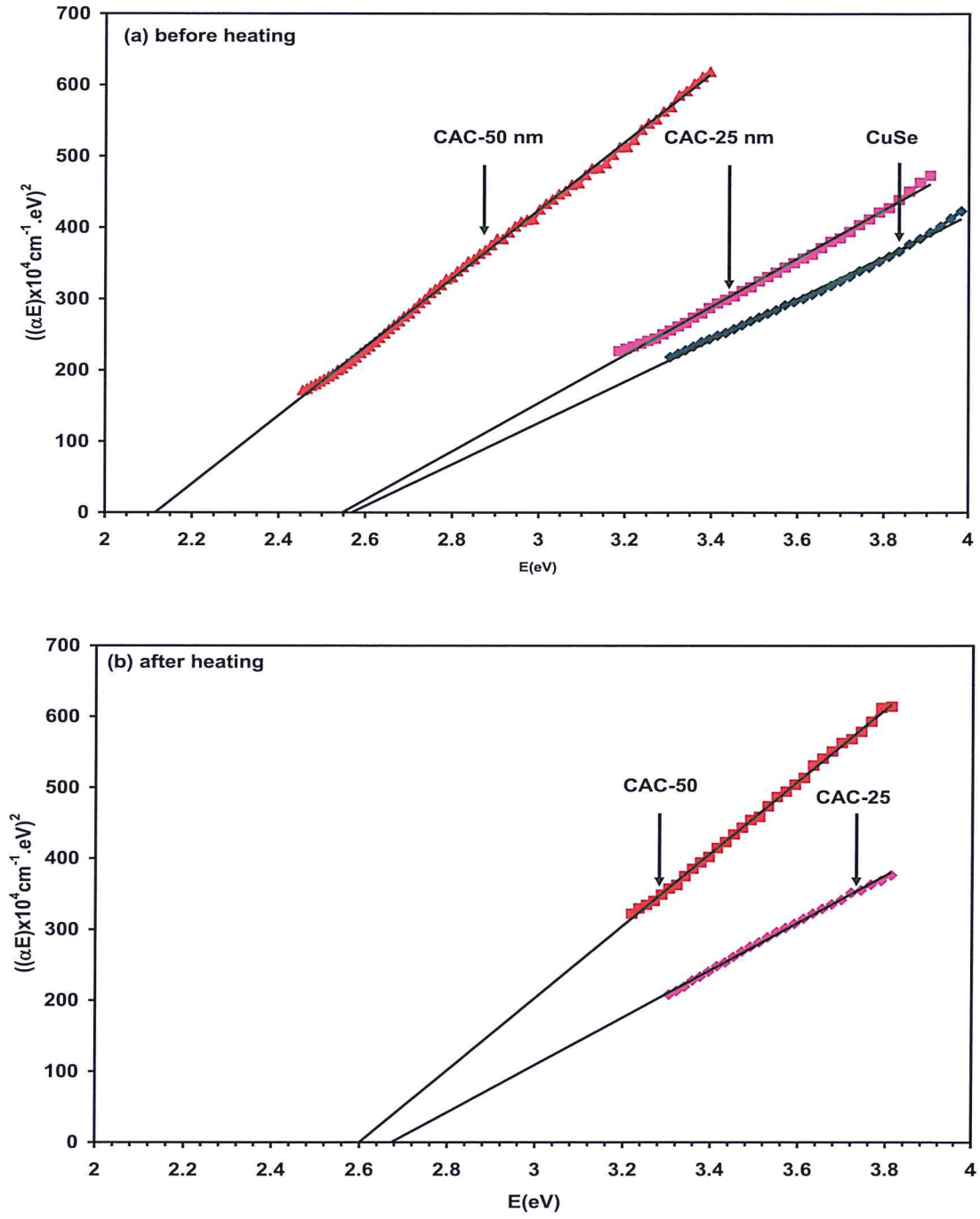
Figure 4. 11 :The Tauc's equation presentation for (a) CuSe ,CAC-25 nm and CAC-50 nm films at room tempreture and (b) CAC-25 nm and CAC-50 nm films after annealing

4.3 Dielectric properties

The optical properties of materials provide an important tool for studying the dielectric performance. Depending on experimental measurements we deduce the dielectric constant for CuSe, CAC-25nm and CAC-50 nm films as function of energy. The real part of the dielectric constant $\acute{\varepsilon}$ which was calculated with the help of equation (2.22) is shown in figure 4.12.

Figure 4.12: The real part of the dielectric constant for CuSe (blue line), CAC-25 nm (pink line), CAC-50 nm (red line) and the best Generalization for the imaginary of Lorentz modeling (blackline).

It is clear from the figure that the high frequency (ω) dielectric constant strongly depends on the thickness of Au layer in the samples. Namely, while $\acute{\varepsilon}$ exhibit value of ~ 1.6 for the two stacked layers of CuSe. It increases to ~ 3.0 value upon insertion of 25 nm Au film. Increasing the Au layer thickness further decreased the values of $\acute{\varepsilon}$ to ~2.3. In addition, it is also noticeable from the Figure

that for incident photon energies less 1.82, 2.18 and 2.14 eV of the CuSe, CAC-25 nm and CAC-50 nm, respectively. The real part of dielectric constant start increasing with decreasing incident photon energy. Such behavior indicates the applicability of CAC samples in IR region of optoelectronical applications. The slope of variation of ε_r with E increases as Au thickness increases. We assign this behavior to the availability of more Au atoms that enhances the electronic polarization in that region. One may see a decrease in values of $\acute{\varepsilon}$ as the energy is increasing to the value ~ 2.04 eV for CuSe and ~ 1.8 eV for CAC-50 nm and to the value ~ 1.51 eV for CAC-25, after that the value of real part increases for both CAC-25 and CAC-50 nm when the frequency approach ~ 2.52 eV before reaching saturation at high frequency.

Also we study the imaginary part of dielectric constant which appears in figure 4.13 for the samples.
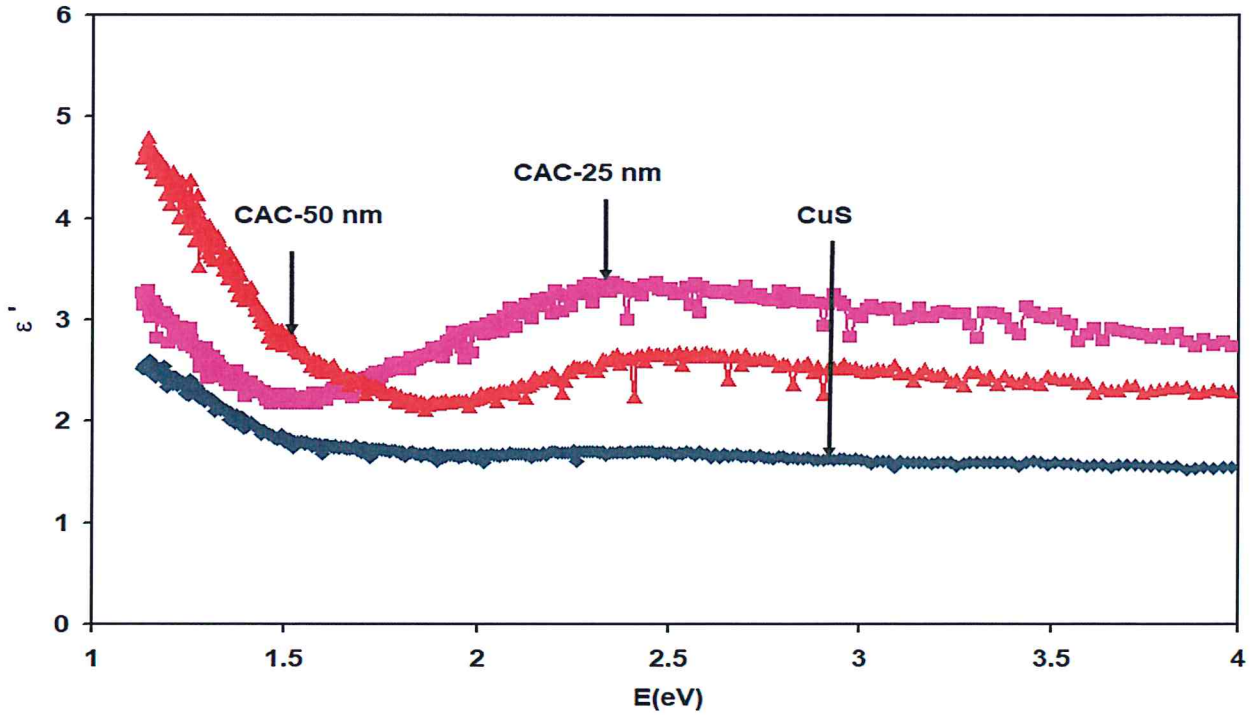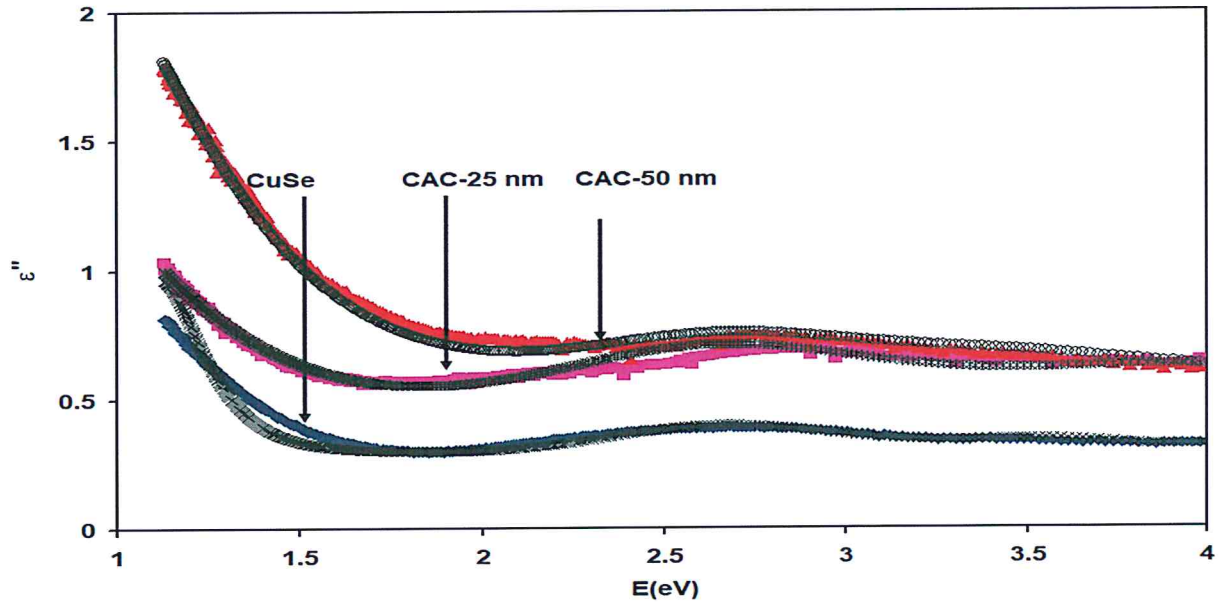

Figure 4.13: the imaginary part of the dielectric constant for CuSe (blue line), CAC-25 nm (pink line), CAC-50 nm (red line) and the best Generalization for the imaginary of Lorentz modeling (black line).

The imaginary part of dielectric constant display constant value in the spectral range of 2.5-4.0 eV.

Its clear that insertion of Au layer increased the value of ε, while there is no effect of Au layer

thickness on the high frequencyε'', the low frequency region steadily increased with decreasing photon energy. Modeling of the imaginary part with Drude-lorentz approach using the equation (2.30) reveal information about the optical conductivity parameters. The good consistency between the theoretical $\tilde{\varepsilon}$ which is shown by dark cross symbol, and the experimentally determined values was achieved via substitutions of the optical conductivity parameters which are shown in Table 4.5.

Table 4.5: The computed parameters of the Plasmon-electron interactions in CuSe, CAC-25 nm and CAC-50 nm films.

	CuSe					CAC-25 nm					CAC-50 nm				
K	1	2	3	4	5	1	2	3	4	5	1	2	3	4	5
τ_i (fs)	0.50	0.61	0.62	0.63	0.90	0.6	0.4	0.41	0.5	0.21	0.45	0.47	0.62	0.80	0.90
ω_{ei} ($\times 10^{15}$ Hz)	1.10	1.40	4.15	5.50	6.59	1.40	9.00	4.15	6.00	6.00	7.81	6.18	3.96	3.96	3.96
n ($\times 10^{17}$ cm^{-3})	1.70	1.70	2.20	2.30	2.30	1.4	1.2	2.2	1	2	2.50	8.80	1.60	1.70	1.60
μ (cm^2/V s)	1.75	2.14	2.18	2.21	3.16	5.19	3.46	3.55	4.33	1.81	5.36	0.86	3.89	3.37	4.33
ω_{pei} (GHz)	3.46	3.46	3.94	3.03	4.03	4.93	1.61	6.18	4.17	5.9	1.40	4.41	5.50	6.07	7.00

Where K is the number of oscillations, ω_{pei} is the Plasmon frequency.

If we use the 1st coulumn (the first oscillation) for each sample for comparison in the Table 4.5, we will see that the table suggests that the insertion of Au layers between two layers of CuSe, significantly, increases the drift mobility of free electrons and the value of the Plasmon frequency as well. Namely, the drift mobility of CuSe increased from 1.75 to 5.19 and reached 5.36 cm^2/ Vs as the Au layer is inserted and it is thickness is increased. The higher the drift mobility, the more suitable the material for optoelectronic applications. The range of Plasmon frequency also extends from 3.46 - 4.03 GHz to 4.95 – 5.9 GHz and to 1.40 – 7.00 GHz as Au layer of thickness of 25 and 50 nm are inserted between layers of CuSe, respectively.

The Plasmon frequency represent limit for the wave reflection in the samples. Its values suggest that these interfaces are more appropriate for production of microwave filters. On the other hand, the decrease in the number of free carrier density (n) upon Au layer insertion is assigned to the e-h recombination processes. Owing to the flowing of holes to the surface of Au layer.

Chapter 5

Conclusions

In this thesis, we have studied the effects of gold nanosandwiching and temperature on the structural and optical properties of CuSe thin films. In general CuSe films exhibit nano –crystallites with needle like shapes. These needles which display length of 1.5 μm before insertion of Au, they exhibit tube like shapes after the insertion of Au layer. The length of the nanotubes reaches 2.5 μm. Structurally, the X-ray diffraction analyses displayed polycrystalline nature of growth with hexagonal lattice. The nanosandwiching of Au layers decreased the grain sizes, increased the strain and defect density. Optically, due to nanosandwiching the absorbability in the visible range increased by more than two times and the band gap shrunk. In addition, an enhancement in the dielectric constant is observed in the IR range upon nanosandwiching of Au between layers of CuSe. Furthermore, the optical conduction parameters presented by scattering time at femtosecond level, free hole density, drift mobility and plasmon frequency are all improved indicating that the CuSe became more appropriate for thin film transistor technology.

Heating the studied samples to 200 C and restudying the structural and optical properties after cooling the samples to room temperature has shown that the heating process increased the crystallites size and improved the crystallinity. The microstrain and defect density also decreased. These enhancements in the structural properties of the films which are achieved via heating are promising as they may indicate more stable optical and dielectric performance of CuSe. As though we strongly advice that the optical and dielectric properties are studied as function of temperature which is one our targets in the future work.

References:

[1]: Amroun, M. N., et al. "Investigation on the structural, optical and electrical properties of mixed SnS2—CdS thin films." Optik-International Journal for Light and Electron Optics 131 (2017): 152-164.

[2] K. Tyagi, B. Gahtori, S. Bathula, M. Jayasimhadri, N.K. Singh, S. Sharma, D. Haranath, A.K. Srivastava, A. Dhar Enhanced thermoelectric performance of spark plasma sintered copper-deficient nanostructured copper selenide J. Phys. Chem. Solids, 81 (2015), pp. 100-105

[3]: Singh, Subhash C., Huiyan Li, Chaonan Yao, Z. Zhan, Weili Yu, Zhi Yu, and Chunlei Guo. "Structural and compositional control in copper selenide nanocrystals for light-induced self-repairable electrodes." *Nano energy* 51 (2018): 774-785.

[4] Nouri, Morteza, H. R. Azimi, Abdolali Moghaddam Saray, and Ramin Yousefi. "S-doping effects on optical properties and highly enhanced photocatalytic performance of Cu3Se2 nanoparticles under solar-light irradiation." *Ceramics International* 43, no. 17 (2017): 14983-14988.

[5] Singh, Subhash C., Huiyan Li, Chaonan Yao, Z. Zhan, Weili Yu, Zhi Yu, and Chunlei Guo. "Structural and compositional control in copper selenide nanocrystals for light-induced self-repairable electrodes." *Nano energy* 51 (2018): 774-785.

[6] Ren, Jie, Yanxia Huang, Yan Liu, and Xiaozhen Tang. "Preparation, characterization and properties of poly (vinyl chloride)/compatibilizer/organophilic-montmorillonite nanocomposites by melt intercalation." *Polymer testing* 24, no. 3 (2005): 316-323.

[7] De Graef, Marc, and Michael E. McHenry. *Structure of materials: an introduction to crystallography, diffraction and symmetry.* Cambridge University Press, 2012.

[8]: Muniz, F. T. L., Miranda, M. A. R., Morilla dos Santos, C., & Sasaki, J. M. (2016). The Scherrer equation and the dynamical theory of X-ray diffraction. Acta Crystallographica Section A: Foundations and Advances, 72(3), 385-390.

[9]: Rekha, K., M. Nirmala, Manjula G. Nair, and A. Anukaliani. "Structural, optical, photocatalytic and antibacterial activity of zinc oxide and manganese doped zinc oxide nanoparticles." Physica B: Condensed Matter 405, no. 15 (2010): 3180-3185.

[10] Das, N. S., P. K. Ghosh, M. K. Mitra, and K. K. Chattopadhyay. "Effect of film thickness on the energy band gap of nanocrystalline CdS thin films analyzed by spectroscopic ellipsometry." Physica E: Low-Dimensional Systems and Nanostructures 42, no. 8 (2010): 2097-2102.

[11]: Yang, Wei, and W. B. Lee. Mesoplasticity and its Applications. Springer Science & Business Media, 2013.

[12]:Saleh, Adli A., A. F. Qasrawi, G. Yumuşak, and A. Mergen. "Physical properties of neodymium tin oxide pyrochlore ceramics." Materials Science-Poland 1, no. ahead-of-print (2017).

[13] Al Garni, S. E., and A. F. Qasrawi. "Effect of Indium nano-sandwiching on the structural and optical performance of ZnSe films." Results in physics 7 (2017): 4168-4173.

[14]: Nair, P. K., Eira Anais Zamudio Medina, Geovanni Vázquez García, Laura Guerrero Martínez, and M. T. S. Nair. "Functional prototype modules of antimony sulfide selenide thin film solar cells." Thin Solid Films 669 (2019): 410-418.

[15] Nagaraja, K. K., S. Pramodini, A. Santhosh Kumar, H. S. Nagaraja, P. Poornesh, and Dhananjaya Kekuda. "Third-order nonlinear optical properties of Mn doped ZnO thin films under cw laser illumination." optical materials 35, no. 3 (2013): 431-439.

[16]: Kissinger, NJ Suthan, M. Jayachandran, K. Perumal, and C. Sanjeevi Raja. "Structural and optical properties of electron beam evaporated CdSe thin films." Bulletin of Materials Science 30, no. 6 (2007): 547-551.

[17]: Dresselhaus, M. S. "Solid State Physics Part II Optical Properties of Solids." (2001).

[18] : Inkson, B. J. "Scanning electron microscopy (SEM) and transmission electron microscopy (TEM) for materials characterization." In Materials characterization using nondestructive evaluation (NDE) methods, pp. 17-43. Woodhead Publishing, 2016.

[19] Shiojiri, Makoto, Chihiro Kaito, Yoshio Saito, Kiyotaka Teranishi, and Sunao Sekimoto. "High resolution electron microscopic study of the growth of Cu-Se crystals by a solid-solid reaction." Journal of Crystal Growth 52 (1981): 883-886.

[20] Jeong, Woo-Lim, Jung-Hong Min, Hae-Sun Kim, Ji-Hun Kim, Jin-Hyeok Kim, and Dong-Seon Lee. "Quantification of effective thermal conductivity in the annealing process of Cu 2 ZnSn (S, Se) 4 solar cells with 9.7% efficiency fabricated by magnetron sputtering." Sustainable Energy & Fuels 2, no. 5 (2018): 999-1006.

[21] Kaviyarasu, K., A. Ayeshamariam, E. Manikandan, J. Kennedy, R. Ladchumananandasivam, Uilame Umbelino Gomes, M. Jayachandran, and M. Maaza. "Solution processing of CuSe quantum dots: Photocatalytic activity under RhB for UV and visible-light solar irradiation." *Materials Science and Engineering: B* 210 (2016): 1-9.

[22]: Liu, Xiaolong, Zhuhua Zhang, Luqing Wang, Boris I. Yakobson, and Mark C. Hersam. "Intermixing and periodic self-assembly of borophene line defects." Nat. Mater 17 (2018): 783-788

[23]: Kavouras, P., I. Ratschinski, G. P. Dimitrakopulos, H. S. Leipner, Ph Komninou, G. Leibiger, and F. Habel. "Deformation and fracture in (0001) and (10-10) GaN single crystals." Materials Science and Technology 34, no. 13 (2018): 1531-1538.

[24]: Garni, S al. "characterization of the au/znse/in/znse/c (ziz) back to back schottky barriers." *Chalcogenide Letters* 14, no. 12 (2017): 545-550.

[25]: Pal, Manoj K., Sandip Dey, Amey P. Wadawale, Nisha Kushwah, Mukesh Kumar, and Vimal K. Jain. "Coordination Polymers of Indium/Copper Selenolates and the Preparation of Metal Selenides." *ChemistrySelect* 3, no. 30 (2018): 8575-8580

[26]: Thieme, Christian, Michael Kracker, Christian Patzig, Katrin Thieme, Christian Rüssel, and Thomas Höche. "The acceleration of crystal growth of gold-doped glasses within the system BaO/SrO/ZnO/SiO2." *Journal of the European Ceramic Society* 39, no. 2-3 (2019): 554-562.

[27]: Sreenu, K., CH Sudhakar Reddy, J. R. Reddy, Radha Velchuri, Suresh Palla, and M. Vithal. "Enhanced photoactivity of antimony phosphates by substitution of H+, Cu 2+ and N 3− in the K 3 Sb 3 P 2 O 14· xH 2 O crystal lattice." Research on Chemical Intermediates 42, no. 6 (2016): 5765-5777.

[28] Vettumperumal, R., S. Kalyanaraman, and R. Thangavel. "Modification of Orientation, Surface and Optical Properties of ZnO Films by Cesium and Erbium Codoping Using Sol–Gel Method." *Journal of Nanoscience and Nanotechnology* 16, no. 9 (2016): 9667-9674.

[29] Kennedy, J., P. P. Murmu, J. Leveneur, A. Markwitz, and J. Futter. "Controlling preferred orientation and electrical conductivity of zinc oxide thin films by post growth annealing treatment." *Applied Surface Science* 367 (2016): 52-58.

[30]: Ponon, Nikhil K., Daniel JR Appleby, Erhan Arac, P. J. King, Srinivas Ganti, Kelvin SK Kwa, and Anthony O'Neill. "Effect of deposition conditions and post deposition anneal on reactively sputtered titanium nitride thin films." Thin Solid Films 578 (2015): 31-37.

[31]: Al Garni, S. E., Olfat A. Omareye, and A. F. Qasrawi. "Growth and characterization of InSe/Ge/InSe interfaces." Optik 144 (2017): 340-347.

[32]: Biju, C. S., S. Suresh, S. Sahaya Jude Dhas, and R. Gowri Shankar Rao. "Effect of lattice strain on the polychromatic emission in ZnO nanostructures for white light emitting diode application." Superlattices and Microstructures 120 (2018): 363-369.

[33]: Khusayfan, Najla M., and Hazem K. Khanfar. "Structural and optical properties of Cu2Se/Yb/Cu2Se thin films." Results in Physics 12 (2019): 645-651.

[34]: Kim, Jae-Eun, Jung Yeol Shin, Hyun-Seok Jang, Jun Woo Jeon, Won G. Hong, Hae Jin Kim, Junhee Choi et al. "Influence of hydrogen incorporation on conductivity and work function of VO 2 nanowires." Nanoscale 11, no. 10 (2019): 4219-4225.

[35] Daldosso, Nicola, and Lorenzo Pavesi. "Nanosilicon photonics." *Laser & Photonics Reviews* 3, no. 6 (2009): 508-534.

[36]: Zhang, Jijun, Linjun Wang, Jiahua Min, Kaifeng Qin, Jian Huang, Ke Tang, Xiaoyan Liang, and Ping Shen. "Annealing of indium-doped CdMnTe single crystals under Cd vapors." Journal of Crystal Growth 358 (2012): 12-15.

[37]: l Garni, S. E., and A. F. Qasrawi. "Effect of Indium nano-sandwiching on the structural and optical performance of ZnSe films." Results in physics 7 (2017): 4168-4173.

[38]: Liu, Yongjun, Menghua Li, and Yourui Suo. "Theoretical study of interaction between atoms of Au, Ag, Cu and clean Si (1 1 1) surface." Surface science 600, no. 24 (2006): 5117-5122.

[39] Lin, Yi, and Duan Yi-Feng. "New infrared properties of the tetragonal CaTiO3." *Chinese Physics Letters* 22, no. 2 (2005): 435.

الملخص

في هذه الأطروحة، تمت دراسة الخصائص الهيكلية والبصرية للأغشية الرقيقة لمادة سيلينيد النحاس التي تم إعدادها بتقنية رقائق بسمك النانو. وعلى وجه الخصوص، تم استخدام طبقات الأغشية الرقيقة الذهبية التي يقل سمكها عن 250 نانومتر كطبقة متوسطة بين طبقتين من مادة سيلينيد النحاس، وقد تمت دراسة تأثير رقائق الذهب على الخواص الهيكلية والبصرية والعازلية لسلينيد النحاس باستخدام حيود الأشعة السينية، المجهر الإلكتروني، وتقنيات الطيف المرئي فوق البنفسجي. بالإضافة إلى ذلك، تمت دراسة تفاصيل microstrain وحجم الحبوب، كثافة التفكك، وأخطاء التراص بالإضافة الى معامل الامتصاص وكذلك فجوة الطاقة وتشتت العازلية. كما تم استكشاف آثار رقائق الذهب على التوصيل باستخدام معادلات Drude-Lorantz. وأظهر تصوير المجهر الألكتروني أن زراعة طبقة من الذهب بين طبقتي سيلينيد النحاس التي تظهر كإبر بطول 1.5 ميكرومتر يحولها إلى أنابيب بطول 2.5 ميكرومترو عرض 220 نانومتر.

وقد أظهرت الدراسة تأثير درجة الحرارة على الهيكلية حيث أن زيادة درجة الحرارة إلى 473 كلفن يزيد من حجم الحبوب ويقلل من كثافة العيوب. أما بصريًا فإنها تزيد من قدرة المادة على امتصاص الضوء بمقدار مرتين وتقلل من فجوة الطاقة كما تحسن ثابت العازلية على التردد العالي وترددات الأشعة تحت الحمراء.

لذلك فإن زراعة طبقة الذهب بين طبقتي سيلينيد النحاس تحسن التوصيل الضوئي مما يجعلها أكثر ملائمة للتطبيقات الالكترونية والبصرية.